The Effects of Macroscopic Disorder in Condensed Matter Systems

Navneeth Ramakrishnan

A THESIS SUBMITTED
FOR THE DEGREE OF
MASTER OF SCIENCE (PHYSICS) BY RESEARCH
AT THE DEPARTMENT OF PHYSICS,
NATIONAL UNIVERSITY OF SINGAPORE

2016

Declaration

I, Navneeth Ramakrishnan, hereby declare that this thesis is my original work and it has been written by me in its entirety. I have duly acknowledged all the sources of information which have been used in the thesis.

This thesis has not been submitted for any degree in any university previously.

Navneeth Ramakrishnan
November 16, 2016

Abstract

The presence of macroscopic disorder in condensed matter systems has been of great experimental and theoretical interest in recent years. In particular, the electrical conductivity and the magnetoconductivity (electrical conductivity in the presence of a magnetic field) are substantially altered due to the presence of macroscopic inhomogeneity. In this work, we investigate the role of disorder in graphene and Dirac semimetals and treat it using an Effective Medium Theory (EMT) formalism. The transverse magnetoresistance (MR) seen in these systems is shown to arise purely as a consequence of the macroscopic inhomogeneities present. Experimental data from graphene and TlBiSSe are used to make both qualitative and quantitative comparisons with the theory presented. We also provide a simple physical intuition that captures the essential physics of disorder induced MR. Lastly, we compare the EMT to an alternative formalism, namely the Random Resistor Network (RRN), and show that the two theoretical models are equivalent.

Acknowledgements

This thesis may only have one author but it would not have been possible without the help and support of many individuals along the way.

First and foremost, I wish to thank Professor Shaffique Adam for giving me an opportunity to work several exciting and interesting projects during my time as his graduate student. His foresight, vision and incredible enthusiasm kept me going, even when the projects were stuck. I am deeply grateful for his mentorship and working under him has truly been a pleasure.

I would also like to thank my collaborators, Indra Yudhishtira, Mirco Milliteri, Lai Ying Tong, Silvia Lara, Jack Hellerstedt, Jinglei Ping and Professor Michael Fuhrer for their support and guidance on various projects. I also wish to thank the extended community at the Center for Advanced 2D Materials and the NUS Physics Department for making my time there enjoyable, challenging and very fulfilling. In particular, I am grateful to Alex Rodin, Alexandra Carvalho, Derek Ho, Fábio Hipólito, Joao Rodrigues, Julien Morin, Keian Noori, Lidia Carvalho, Roland Hablutzel and Vindhiya Prakash for endless physics and non-physics discussions.

Last but not least, I wish to thank my friends and my family for supporting me as they always have.

Contents

Contents ix

List of Figures xi

List of Publications xiii

1 Introduction 1
- 1.1 Overview . . . 1
- 1.2 Outline of Thesis . . . 3

2 Theoretical Background 5
- 2.1 Magnetoresistance . . . 5
  - 2.1.1 Semi-classical MR . . . 7
  - 2.1.2 Homogeneous two channel model . . . 8
  - 2.1.3 Disordered one channel model . . . 11
  - 2.1.4 Effective Medium Theory . . . 15
  - 2.1.5 Analytical two channel model result and the EMT . . . 18
- 2.2 Impurity scattering and transport . . . 20

3 Graphene 25
- 3.1 Introduction to graphene . . . 25
- 3.2 Theoretical background . . . 26
- 3.3 Comparison with experiment . . . 31

4 Dirac Semimetals 35
- 4.1 Review of Dirac Semimetals . . . 35
- 4.2 Hamiltonian and electronic properties . . . 36
- 4.3 Coulomb impurities and Boltzmann conductivity . . . 38
- 4.4 Disorder and 3D EMT equations . . . 40
- 4.5 Results . . . 44

5 Universality of disorder induced MR 51

5.1 The Random Resistor Network (RRN) 51
5.2 Comparison with the EMT 54
5.3 Experimental use 56

6 Conclusion **59**
6.1 Summary 59
6.2 Future work 60

A Sample EMT code **63**

B Sample RRN code **65**

Bibliography **71**

List of Figures

2.1 Schematic diagram of the Hall Effect 7
2.2 Simple two puddle model 12
2.3 Origin of MR in a two puddle model 15

3.1 The band structure of graphene 26
3.2 Experimental evidence for the presence of disorder in graphene 28
3.3 Experimental MR vs B curves for graphene 31
3.4 Dependence of the quadratic MR coefficient of graphene on disorder . . . 32

4.1 Band structure of the Dirac semimetal Cd_3As_2 36
4.2 RPA Polarization function in three dimensions 39
4.3 Carrier density fluctuations and formation of puddles in Na_3Bi 41
4.4 Conductivity versus carrier density theory curves 45
4.5 Mobility versus carrier density in TlBiSSe 47
4.6 Magnetoresistance in TlBiSSe 48

5.1 The Random Resistor Network of four terminal resistors 52
5.2 The even odd effect seen for finite network sizes in the RRN 53
5.3 Schematic of the quadratic to linear MR transition 54
5.4 Collapse of the EMT and RRN models onto a single universal curve . . . 55
5.5 Quadratic MR coefficient mapping between EMT and RRN 57

List of Publications

1. Jinglei Ping, Indra Yudhistira, Navneeth Ramakrishnan, Sungjae Cho, Shaffique Adam, and Michael S Fuhrer. Disorder-induced magnetoresistance in a two-dimensional electron system. *Phys. Rev. Lett.,* ***113*** *047206*, 2014. [1]

2. Navneeth Ramakrishnan, Mirco Milletari, and Shaffique Adam. Transport and magnetotransport in three-dimensional Weyl semimetals. *Phys. Rev. B,* ***92*** *245120*, 2015. [2]

3. Jack Hellerstedt, Mark T Edmonds, Navneeth Ramakrishnan, Chang Liu, Bent Weber, Anton Tadich, Kane M O'Donnell, Shaffique Adam, and Michael S Fuhrer. Electronic properties of high-quality epitaxial topological dirac semimetal thin films. *Nano Lett.,* ***16*** *5 3210*, 2016. [3]

4. Navneeth Ramakrishnan, Ying Tong Lai, Silvia Lara, and Shaffique Adam. Universality of disorder induced magnetoresistance. *in preparation.* [4]

Chapter 1

Introduction

1.1 Overview

This thesis examines the effects of disorder on conductivity and magnetoresistance in various condensed matter systems. More specifically, we examine a variety of semi-classical effects that arise due to the presence of macroscopic spatial disorder in these systems. The following broad topics are addressed in this work:

The idea of magnetoresistance (MR), where the electrical resistance of a material changes with an external magnetic field, has been of theoretical and experimental interest for a very long time. However, despite its age, the many faceted nature of MR means that it is an extremely important research topic even today with hundreds of papers on the subject being written each year. Key developments such as the Nobel Prize of 2007 going to the discovery of giant magnetoresistance [5], technological applications of MR in memory storage devices and the emergence of MR as a great experimental probe to characterize materials show that we are far from relegating MR to the textbooks just yet. We examine various mechanisms that lead to semi-classical magnetoresistance in condensed matter physics such as the presence of multiple "channels" of charge carriers as well as varying carrier concentrations and conductivities across a sample. We also derive some simple physical results that intuitively explain the origin of MR due to disorder.

A second important piece of this story is the development of "effective" models that characterize disorder. Disorder in condensed matter systems consists of two related ideas: The

first is the presence of impurities or defects in a crystal. This breaks the discrete translational symmetry of the lattice and scattering off of these impurities determines the magnitude of conductivity in these systems. We will later review the Boltzmann conductivity formalism which measures the effect of such scattering on the conductivity. There is a second sense in which a material is said to be disordered and this is macroscopic disorder, which is the focus of this thesis. A sample is said to be macroscopically disordered when it is a composite structure that consists of several regions, and each region has a uniform and distinct conductivity. As early as the 1930s, Bruggerman [6] had developed a technique known as the Effective Medium Theory (EMT) to understand and calculate the effective conductivity of such a composite structure. This work was then refined by Landauer [7], Stroud [8], Adam [1] and others over the years, including work as recent as in 2015 [2]. An alternative way to treat this macroscopic disorder was developed by Parish and Littlewood who proposed the idea of a Random Resistor Network (RRN) that accurately modeled conductivity in materials such as silver chalcogenides [9]. The sense in which the two ideas are related is when one considers impurities with long range potentials e.g. charged impurities - these are capable of causing scattering events and also lead to the formation of macroscopic disorder as we shall see later on.

Finally, we take a close look at two experimental systems in this thesis: graphene and Dirac semimetals. The discovery of graphene in 2004 [10] marked an important turning point in condensed matter physics. The dynamics of electrons and holes in graphene were correctly described by the Dirac equation instead of the Schrodinger equation due to the linear dispersion relation close to the so-called Dirac points in the band structure of graphene. Interesting electrical properties such as the universal minimum conductivity, high mobilities at room temperature and so on evoked much theoretical and experimental interest in graphene. The three dimensional analogue of the band structure of graphene was recently discovered in materials such as Na_3Bi, TlBiSSe and Cd_3As_2 which are called Dirac semimetals or Weyl semimetals in the literature. Experimental work has shown that disorder plays an important role in determining the electrical properties of both graphene and Dirac semimetals.

In this work, we shall combine the three topics introduced above to examine the effects of macroscopic disorder in graphene and Dirac semimetals using the Effective Medium Theory, both in the absence and presence of an external magnetic field. We shall also

compare the Effective Medium Theory with the alternative Random Resistor Network formalism.

1.2 Outline of Thesis

This thesis is organized into the following chapters.

Chapter 2: Theoretical Background - This chapter introduces the concept of magnetoresistance, including an overview of past and present research in this field. We then turn our attention to the specific mechanisms of semi-classical MR that are of interest in this work and elaborate on the theoretical background for these including simple intuitive models and the full EMT approach. Lastly, we introduce the Boltzmann equation within the relaxation time approximation to calculate conductivity, which then serves as the input to the EMT.

Chapter 3: Graphene - In this chapter, we introduce graphene and focus on the low energy physics near the Dirac points. We then show experimental evidence of disorder in graphene that justifies the use of the EMT. Using the Boltzmann conductivity as the input, we calculate the magnetoresistance and compare it with experimental samples. In particular, we examine the quadratic coefficient of magnetoresistance and how this low field MR persists due to disorder, even in a one channel model. The results here have been published in Ref. [1].

Chapter 4: Dirac semimetals - After an introduction to the relatively new field of Dirac semimetals, we derive the basic electronic properties of these materials from the low energy Hamiltonian. We then derive the Boltzmann conductivity and discuss how to treat the screening of charged impurities by the carriers. Finally, we show experimental evidence for the presence of disorder and therefore introduce the 3D EMT equations here. We compare both conductivity and MR with experimental results in TlBiSSe. The results here have been published in Ref. [2] and Ref. [3].

Chapter 5: The Random Resistor Network and the Effective Medium Theory - We introduce the concept of the Random Resistor Network developed by Ref. [9] and compare it with the EMT. We discover that the MR vs B curves of the two models, when appropriately scaled, collapse onto a single universal curve. The equivalence of these two models and its consequence to experimentalists is briefly discussed. The results here have been published in Ref. [4].

Chapter 6: Conclusion - We summarize the key findings contained in this thesis and propose an outlook for future research.

Chapter 2

Theoretical Background

2.1 Magnetoresistance

Magnetoresistance (MR) is defined as the change in electrical resistance due to the application of a magnetic field and is given by the following relationship.

$$MR = \frac{\rho(B) - \rho(0)}{\rho(0)}. \tag{2.1}$$

Here, $\rho(B)$ is the electrical resistivity at a given magnetic field B. Magnetoresistance remains an extremely active research topic with hundreds of papers being written every year. There are so many mechanisms that lead to interesting MR effects that it is futile to attempt to capture it all. We give a brief overview following Ref. [11] on a possible classification of MR although the list here is not exhaustive.

Ordinary magnetoresistance (OMR) refers to the most common type of MR and was discovered by Lord Kelvin. This is a result of carriers being deflected due to the classical Lorentz force and we shall discuss this in detail in Sec. 2.1.1. OMR is always positive and can be observed at high temperatures due to its classical origins whereas a lot of the other quantum MR mechanisms are washed out by temperature.

Anisotropic magnetoresistance (AMR) was also first discovered by Kelvin [12] and strongly depends on the angle made by the magnetic field with the electric current. Electrical resistance is maximized when the two fields are parallel in contrast to OMR where the MR is zero when the two fields are parallel. The mechanism behind AMR is a combination of spin orbit interaction and d-band splitting [13, 14] although there may be material dependent properties including the dimensions of the sample that contribute to this effect.

Thin film structures that consist of magnetic and nonmagnetic conducting layers result in giant magnetoresistance (GMR) [15, 16]. The key mechanism here is the spin dependent scattering of electrons due to the alignment of the magnetization of adjacent magnetic layers. The magnetization alignment of the two layers can be controlled using an external magnetic field. Transition metals such as Fe, Co and Ni are ideal candidates to observe GMR due to the large energy gap between the spin up and spin down 3d bands. The discovery of GMR by Fert and Grunberg was awarded the 2007 Nobel Prize and this phenomenon is the basis of magnetic field sensors, which are used in electronic devices such as microelectromechanical sensors, hard disks etc [17].

Yet another quantum mechanical MR mechanism is tunneling magnetoresistance (TMR) [18–20]. In this case a pair of electrodes are separated by thin insulating barrier and the magnetization of the electrodes is fixed by an external field. When the two electrodes have parallel magnetization, the probability of tunneling is much higher and the resistance is therefore much lower. This yields an on state and an off state with very low resistance and very high resistance respectively, that can be controlled by the external field.

A currently unexplained mechanism of MR is the one that leads to colossal magnetoresistance (CMR). In certain manganite perovskites, one finds that the resistance can change by several orders of magnitude. Current hypotheses suggest that the reason could be the interplay between electron phonon coupling and a magnetic phase transition but the full quantitative understanding remains a topic of current research.

The banner of MR also includes phenomena such as weak localization (WL) and weak anti-localization (WAL) which occur due to quantum interference [21] of the electron's possible paths around a magnetic impurity. This manifests itself only at low temperatures and can also lead to negative MR. Other mechanisms for negative MR include magnetic

transitions brought on by heat treatments on certain materials [22] and possibly electron-electron interactions [23, 24]. At very high magnetic fields, where quantization leads to the formation of Landau levels, one again comes across interesting MR physics. Abrikosov's quantum magnetoresistance [25] is a type of MR that occurs in gapless semiconductors in the Landau level regime. Similarly, the Shubnikov - de Haas (SdH) effect is also seen in this regime.

2.1.1 Semi-classical MR

Given that there are so many different MR mechanisms, it may seem surprising to restrict ourselves to one. However, for the materials we are going to consider, we only need to concern ourselves with OMR that occurs due to transverse magnetic fields. While it is possible to observe longitudinal magnetoresistance, SdH oscillations, WL and WAL and so on in graphene [26] and Dirac semimetals [3, 27], these effects either require very high magnetic fields or low temperatures. In the absence of these conditions, the transverse OMR remains dominant [1, 3, 27] and this shall be the focus of the remaining chapters.

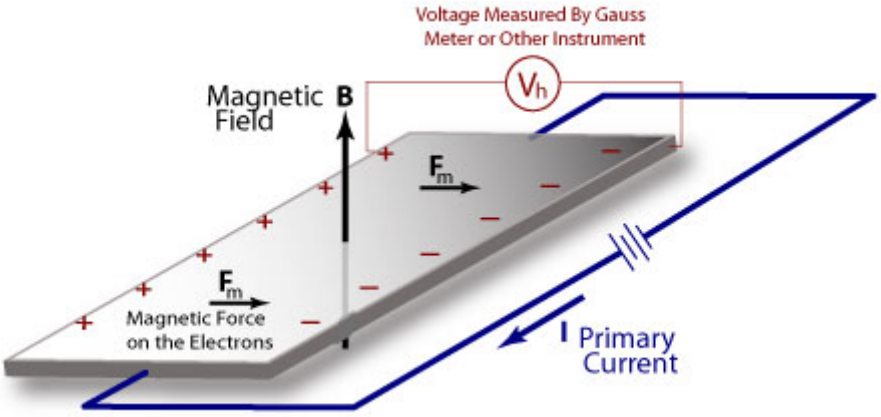

FIGURE 2.1: The applied magnetic field produces a Lorentz force that initially deflects electrons. However, in the steady state, the Hall field precisely cancels out the Lorentz force giving no MR. Image courtesy Ref. [28]

The OMR we consider is referred to as semi-classical because it arises where the MR mechanism itself is classical while the conductivity of the sample may be calculated through semiclassical approaches such as the Boltzmann formalism.The cause of semi-classical MR is fundamentally due to the Lorentz force that deflects moving charge carriers

from their path. A well known example of transverse MR (although in this case, the MR is identically zero in the steady state) is the Hall Effect which is schematically described in Fig. 2.1. In this case, the build up of electrons along the edge of the sample due to the Lorentz force results in a Hall field. The Hall field in the steady state precisely cancels the Lorentz force thereby resulting in no more deflections in the path of the charge carriers and therefore, no observable MR. However, the Hall effect assumes a homogeneous sample. Various types of disorder can lead to deviations from the Hall Effect results and these will be elaborated below.

2.1.2 Homogeneous two channel model

Assume the same physical situation shown in Figure 2.1. Now, we consider the case where both electrons and holes are present in the sample.

We enforce the steady state conditions where the current along the x direction must take a constant value and the current along the y direction is zero at any point on the conductor. The only solution to this is for each carrier to travel in straight lines at constant velocity. We assume angles θ and ϕ for the angle that the velocities of the electrons and holes respectively make with respect to their zero field trajectories. They must satisfy the equilibrium condition $\frac{dv}{dt} = 0$ since this is a steady state.

Let the electron concentration be n^e and hole concentration be n^h. We can define conductivity matrices for each charge carrier that relate the current density with the electric fields.

$$\begin{pmatrix} J_x \\ J_y \end{pmatrix} = \begin{pmatrix} \sigma_{xx} & \sigma_{xy} \\ \sigma_{yx} & \sigma_{yy} \end{pmatrix} \begin{pmatrix} E_x \\ E_y \end{pmatrix}. \tag{2.2}$$

Note that in the situation corresponding to Figure 2.1, E_x is simply the applied electric field while E_y is the Hall field that arises in the sample due to the magnetic field. Consider the dynamics of the carriers due to the electric and magnetic fields and a drag force. Solving for $\frac{dv}{dt} = 0$, the steady state, we have the following form for the conductivity matrices for electrons and holes and they are independent of each other.

$$\sigma^e = \frac{n^e e\mu}{1 + (\mu B)^2} \begin{pmatrix} 1 & \mu B \\ -\mu B & 1 \end{pmatrix}, \tag{2.3}$$

$$\sigma^h = \frac{n^h e\mu}{1+(\mu B)^2}\begin{pmatrix} 1 & -\mu B \\ \mu B & 1 \end{pmatrix}. \tag{2.4}$$

Here, μ is the mobility (which is determined by the drag force due to collisions) and is assumed equal for both electrons and holes, e is the electronic charge and B is the applied magnetic field in the direction shown. Now, we enforce the steady state condition $J_y^{total} = 0$. Thus, we have

$$\begin{aligned} J_y^{total} &= J_y^e + J_y^h \\ 0 &= \frac{n^e e\mu}{1+(\mu B)^2}(-\mu B E_x + E_y) + \frac{n^h e\mu}{1+(\mu B)^2}(\mu B E_x + E_y) \\ 0 &= (n^e + n^h)E_y - (n^e - n^h)\mu B E_x \\ E_y &= \alpha \mu B E_x. \end{aligned} \tag{2.5}$$

Here, $\alpha = \frac{n^e - n^h}{n^e + n^h}$. We now have the Hall field in terms of the applied electric field and B. We now look at θ and ϕ.

Using the previous result, we can express J_y^e and J_x^e only in terms of the applied electric field E_x.

$$\begin{aligned} \tan(\theta) &= \frac{J_y^e}{J_x^e} \\ &= \frac{\sigma_{yx}^e E_x + \sigma_{yy}^e E_y}{\sigma_{xx}^e E_x + \sigma_{xy}^e E_y} \\ &= \frac{\sigma_{yx}^e E_x + \sigma_{yy}^e \alpha \mu B E_x}{\sigma_{xx}^e E_x + \sigma_{xy}^e \alpha \mu B E_x} \\ &= \frac{\mu B(\alpha - 1)}{1 + \alpha(\mu B)^2}. \end{aligned} \tag{2.6}$$

Similarly, the result for holes is

$$\begin{aligned} \tan(\phi) &= \frac{J_y^h}{J_x^h} \\ &= \frac{\mu B(\alpha + 1)}{1 - \alpha(\mu B)^2}. \end{aligned} \tag{2.7}$$

Without loss of generality, we assume (for the rest of this paragraph) that $n^e \geq n^h$ i.e. $0 \leq \alpha \leq 1$. We see that while the magnitude of θ goes from 0 to $\frac{\pi}{2}$, the angle ϕ can go from 0 to π. This is because the denominator of that fraction changes sign as we increase B. In other words, for a sufficiently large magnetic field, the minority charge carriers reverse direction and travel against the force applied by the electric field. The saturation value of the magnetoresistance will be shown to be the case when $\phi = \pi$. Now, we calculate J_x for electrons.

$$\begin{aligned} J_x^e &= \sigma_{xx}^e E_x + \sigma_{xy}^e E_y \\ &= \frac{n^e e\mu}{1+(\mu B)^2}\left(1+\alpha(\mu B)^2\right) E_x. \end{aligned} \tag{2.8}$$

Since $|\alpha| \leq 1$, we always see that $J_x(B) \leq J_x(0)$ i.e. we have MR. Note that we recover the result of the Hall effect (i.e. no change in J_x^e with B) in the case of $\alpha = 1$. In the limit of $\mu B \gg 1$, assuming $\alpha \neq 0$, we get the saturation value

$$J_x^e = n^e e\mu\alpha E_x. \tag{2.9}$$

Similarly, the equation for holes is

$$J_x^h = \frac{n^h e\mu}{1+(\mu B)^2}\left(1-\alpha(\mu B)^2\right) E_x. \tag{2.10}$$

Note that we recover the result of the Hall effect (i.e. no change in J_x^h with B) in the case of $\alpha = -1$. The total current is

$$J_x^{total} = \frac{(n^e+n^h)e\mu}{1+(\mu B)^2}\left(1+\alpha^2(\mu B)^2\right) E_x. \tag{2.11}$$

The Taylor expansion of MR clearly has no linear term in B. The first nonzero coefficient of MR is the quadratic coefficient and it goes as $A = (1-\alpha^2)$. In the limit of $\mu B \gg 1$, assuming $\alpha \neq 0$, we get

$$J_x^h = -n^h e\mu\alpha E_x. \tag{2.12}$$

Clearly, under high B field, there is a saturation value for the magnetoresistance that is independent of B. Note also that the reversal in the sign of J_x for the minority charge carrier is clearly seen here. In total we have

$$J_x^{total} = (n^e - n^h)e\mu\alpha E_x. \tag{2.13}$$

Finally, if $\alpha = 0$, that is if the electron and hole concentrations are equal, we get $J_x^{total} \to 0$ as $\mu B \gg 1$. Thus, the magnetoresistance does not saturate in this case.

Lastly, for completeness, we also give the expression for J_y as a function of E_x and B. It is

$$J_y^h = \frac{n^h e\mu}{1 + (\mu B)^2} (1 + \alpha) \mu B E_x, \tag{2.14}$$

$$J_y^e = \frac{n^e e\mu}{1 + (\mu B)^2} (-1 + \alpha) \mu B E_x. \tag{2.15}$$

Indeed, $J_y^{total} = 0$ for all B and this is merely the steady state condition that was imposed.

In summary, we see that the presence of a second channel of a charge carrier with a different sign resulted in magnetoresistance that was saturating (except in the special case of $n^e = n^h$).

2.1.3 Disordered one channel model

In this section, we take a slightly different type of disorder into account. Section. 2.1.2 assumed homogeneous carrier concentrations but with two types of carriers in the entire sample. Now, we shall assume spatial variations of carrier concentration in the sample. In the literature, this type of spatially varying carrier concentration is called "puddling". We shall assume a single type of charge carrier (say electrons) and that we have two puddles with charge concentrations n_1 and n_2 and the two puddles are arranged as shown in Figure. 2.2. The argument that follows can be easily adapted for more regions but the

aim here is to build the intuition before using the Effective Medium Theory for a proper treatment.

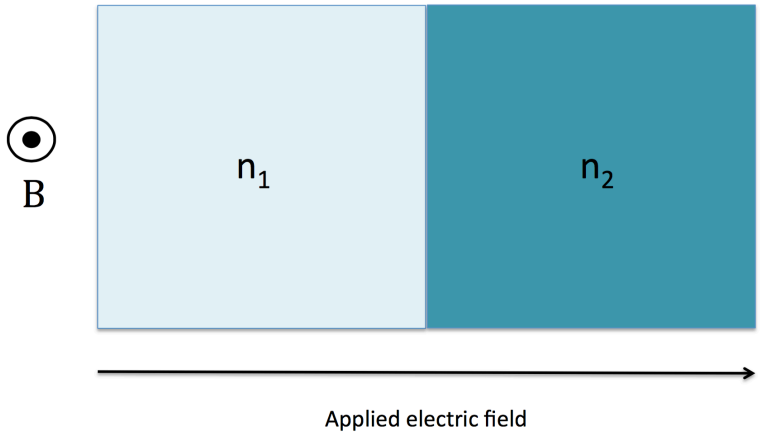

FIGURE 2.2: Assume a sample with two different carrier concentrations of electrons in two regions. The magnetic field is out of the plane of the sample and the applied electric field is along the x direction as shown.

In the presence of a magnetic field through the plane of the sample, the velocity of the electrons is related to the field by

$$\begin{pmatrix} v_x \\ v_y \end{pmatrix} = -\frac{\mu}{1+\mu^2 B^2} \begin{pmatrix} 1 & -\mu B \\ \mu B & 1 \end{pmatrix} \begin{pmatrix} E_x \\ E_y \end{pmatrix}. \tag{2.16}$$

Note now, that the E_x is the local electric field in that region and is different from the applied electric field, even when there is no magnetic field. We enforce the first steady state condition $n_1 e v_1^x = n_2 e v_2^x = J_x$.

$$\begin{aligned} J_x &= \frac{n_1 e\mu}{1+(\mu B)^2}(E_1^x - \mu B E_1^y) \\ \therefore\ E_1^x &= \frac{J_x}{n_1 e\mu}(1+\mu^2 B^2) + \mu B E_1^y. \end{aligned} \tag{2.17}$$

Similarly, one gets

$$E_2^x = \frac{J_x}{n_2 e\mu}(1+\mu^2 B^2) + \mu B E_2^y. \tag{2.18}$$

Now, we enforce the second steady state condition $J_y^{total} = 0$. Thus, we have,

$$\begin{aligned} J_y^{total} &= J_y^1 + J_y^2 \\ 0 &= \frac{n_1 e\mu}{1+(\mu B)^2}(\mu B E_1^x + E_1^y) + \frac{n_2 e\mu}{1+(\mu B)^2}(\mu B E_2^x + E_2^y). \end{aligned} \tag{2.19}$$

We assume a solution where E_y is independent of n, i.e. it is a global parameter that only depends on the electron build up at the edge that produces the Hall field. This is consistent with the idea that the charge buildup along the edge is uniform and that there cannot be clusters of charge at the edge. Using (2.17) and (2.18), we get

$$E_y = -\frac{\mu B J_x}{n_{avg} e\mu}. \tag{2.20}$$

Thus, we have

$$\begin{aligned} E_1^x &= \frac{J_x(1+\mu^2 B^2)}{n_1 e\mu} + \mu B E^y \\ &= \frac{J_x(1+\mu^2 B^2)}{n_1 e\mu} - \frac{\mu^2 B^2 J_x}{n_{avg} e\mu} \\ &= \frac{J_x}{n_1 e\mu} + \frac{J_x \mu^2 B^2}{e\mu}\left(\frac{1}{n_1} - \frac{1}{n_{avg}}\right) \\ &= \frac{J_x}{n_1 e\mu} + \frac{J_x \mu^2 B^2}{e\mu}\left(\frac{-\alpha}{n_1}\right). \end{aligned} \tag{2.21}$$

As before, we have defined $\alpha = (n_1 - n_2)/(n_1 + n_2)$. For the other puddle we have

$$E_2^x = \frac{J_x}{n_2 e\mu} + \frac{J_x \mu^2 B^2}{e\mu}\left(\frac{\alpha}{n_2}\right). \tag{2.22}$$

Finally, we can express the velocities v_x and v_y for each puddle as follows.

$$v_i^x = \frac{-J_x}{n_i e}. \tag{2.23}$$

We also have, for $i = 1, 2$

$$\begin{aligned} v_i^y &= \frac{-\mu}{(1+\mu^2B^2)}(\mu B E_i^x + E^y) \\ &= \frac{-\mu}{(1+\mu^2B^2)}\left(\mu B(\frac{J_x}{n_i e\mu}(1+\mu^2B^2) + \mu B E_1^y) - \frac{\mu B J_x}{n_{avg} e\mu}\right) \\ &= \frac{-\mu}{(1+\mu^2B^2)}\left(\mu B(\frac{J_x}{n_i e\mu}(1+\mu^2B^2) - \mu B\frac{\mu B J_x}{n_{avg} e\mu}) - \frac{\mu B J_x}{n_{avg} e\mu}\right) \\ &= \left(\frac{\mu B J_x}{n_a e} - \frac{\mu B J_x}{n_i e}\right). \end{aligned} \tag{2.24}$$

To calculate J_x in terms of J_0, the zero field current, we realize that the electric field across the sample may be redistributed over the puddles but the net change in electric field due to the applied B field must be zero, since the total voltage across a sample cannot change due to a magnetic field. Thus, we have from (2.21) and (2.22)

$$\begin{aligned} &E_1^x(B=0) + E_2^x(B=0) = E_1^x(B\neq 0) + E_2^x(B\neq 0) \\ &\frac{J_0}{n_1 e\mu} + \frac{J_0}{n_2 e\mu} = \frac{J_x}{n_1 e\mu} + \frac{J_x\mu^2B^2}{e\mu}\left(\frac{1}{n_1} - \frac{1}{n_{avg}}\right) + \frac{J_x}{n_2 e\mu} + \frac{J_x\mu^2B^2}{e\mu}\left(\frac{1}{n_2} - \frac{1}{n_{avg}}\right) \\ &\frac{J_0}{e\mu}\left(\frac{n_1+n_2}{n_1 n_2}\right) = \frac{J_x}{e\mu}\left[\frac{n_1+n_2}{n_1 n_2} + \mu^2B^2\left(\frac{n_1+n_2}{n_1 n_2} - \frac{4}{n_1+n_2}\right)\right] \\ &J_0 = J_x(1+\alpha^2\mu^2B^2). \end{aligned} \tag{2.25}$$

For small B, we do a Taylor expansion and find our final result to be

$$J_x = J_0(1-\alpha^2\mu^2B^2). \tag{2.26}$$

Again, there is no linear coefficient in B when we do a Taylor expansion of MR. As this result will be of significance later, we draw attention to the fact that unlike the two channel model, the MR in the disordered one channel model shows a quadratic coefficient A that goes as

$$A \sim \alpha^2 = \left(\frac{n_1 - n_2}{n_1 + n_2}\right)^2. \tag{2.27}$$

Thus, we see the origin of magnetoresistance from a simple two puddle model.

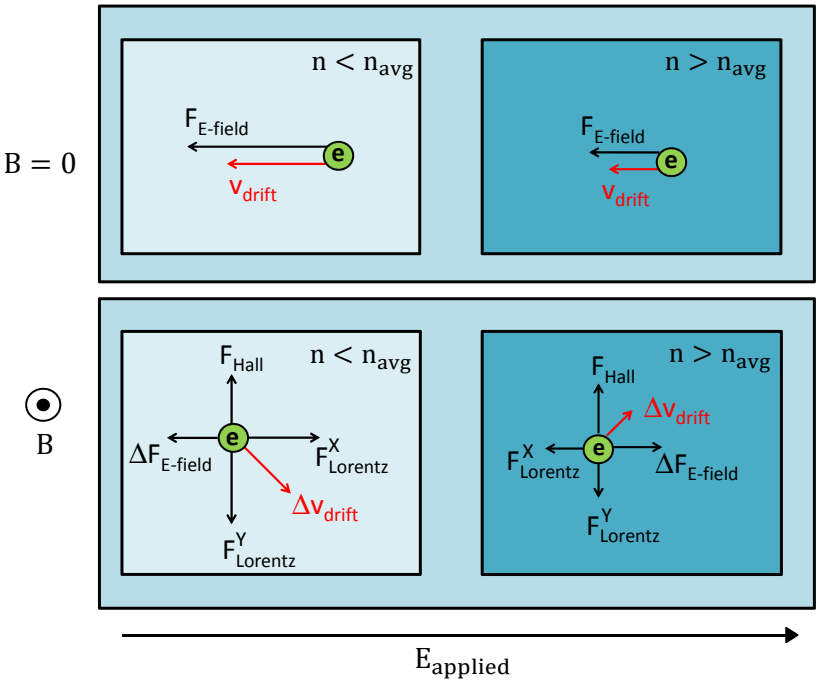

FIGURE 2.3: Consider two regions where the carrier density is larger and smaller than the average carrier density of the sample respectively. The effect of a magnetic field is to introduce a component of the Lorentz force against the direction of travel of the electrons in both regions. This is the origin of magnetoresistance in a simple two puddle model. Image from Ref. [1]

Figure 2.3 illustrates the result that we have derived. Essentially, the electrons in the case of the Hall effect had a Lorentz force that was precisely balanced by the Hall field. However, now, the Lorentz force varies between regions (due to different carrier drift velocities) and hence, the global Hall field cannot balance the locally varying Lorentz force anymore - it can only do so in an averaged sense. Thus, the electrons travel in a zigzag fashion and this causes a component of the Lorentz force to act against the drift velocity, in both regions. The result is a net decrease in drift velocity and this is seen as magnetoresistance.

2.1.4 Effective Medium Theory

We now have the intuition behind why disorder leads to MR. The formalism to tackle such macroscopic disorder is the Effective Medium Theory. It has been refined over the

years including by the present author and we give a brief derivation following Ref. [29] for the two dimensional case.

Consider a two dimensional sheet of material which is a composite of N areas each with conductivity σ_i, where $i = 1, \cdots, N$. The area fraction of the i^{th} puddle is denoted by f_i. We wish to calculate the effective conductivity of this sheet. Each puddle is thought to be embedded in a homogeneous effective medium that has some conductivity σ_E which is yet to be determined. The applied electric field is $\vec{E}_0$. We first work out the electric field $\vec{E}_i$ inside each puddle. The self consistency condition for the EMT is the simple requirement that the average electric field through the puddles be the same as the applied external electric field i.e.

$$\sum_{i=1}^{N} f_i \vec{E}_i = \vec{E}_0. \tag{2.28}$$

Each puddle is treated individually and is assumed to be embedded in the same effective homogeneous medium of conductivity σ_E through which the electric field is $\vec{E}_0$. Consider the i^{th} puddle embedded in the effective medium. For simplicity, we assume that all puddles are circular of some radius a and we now work out $\vec{E}_i$. $\vec{E}_0 = E_0\vec{e}_x$ is the applied electric field. Assuming that the puddle possesses a uniform polarization (i.e. dipole moment per unit area) $\vec{M}$ pointing in the same direction as the external field, so that $\vec{M} = M\vec{e}_x$, it is a well known result of electrostatics that the electric field outside the region due to this polarization is given by [30]

$$\vec{E}_{pol}(\vec{r}) = \frac{a^2}{2\epsilon_0 r^2}\left[2(\vec{M}\cdot\vec{e}_r)\vec{e}_r - \vec{M}\right], \tag{2.29}$$

with a corresponding potential

$$U_{pol}(\vec{r}) = \frac{a^2}{2\epsilon_0}\frac{M}{r}\cos(\theta). \tag{2.30}$$

The total field outside ($r > a$) in polar coordinates is obtained by taking the $\vec{e}_r$ components,

$$\begin{aligned} E_{E,r}(r,\theta) &= E_{0,r} + E_{pol,r} \\ &= E_0\cos(\theta) + \frac{a^2}{2\epsilon_0 r^2}M\cos(\theta), \end{aligned} \tag{2.31}$$

and the potential is

$$U_E(r,\theta) = -E_0 r\cos(\theta) + \frac{a^2}{2\epsilon_0}\frac{M}{r}\cos(\theta). \tag{2.32}$$

Next, we consider the field inside the puddle. With the ansatz that the field inside is proportional to the externally applied field $\vec{E}_0$, we get

$$\begin{aligned} \vec{E}_i &= C\vec{E}_0 \\ &= CE_0\vec{e}_x \\ &= CE_0\cos(\theta)\vec{e}_r, \end{aligned} \tag{2.33}$$

with potential

$$U_i(r,\theta) = -CE_0 r\cos(\theta). \tag{2.34}$$

At the boundary, we have

$$U_E(a,\theta) = U_i(a,\theta) \tag{2.35}$$

and

$$\sigma_E E_{E,r} = \sigma_i E_{i,r}. \tag{2.36}$$

We can make use of these to solve for M and C. This yields

$$C = \frac{2\sigma_E}{\sigma_E + \sigma_i} \tag{2.37}$$

and

$$M = 2\epsilon_0 E_0\left(\frac{2\sigma_E}{\sigma_E+\sigma_i} - 1\right). \tag{2.38}$$

We conclude that

$$E_i = \left(\frac{2\sigma_E}{\sigma_E+\sigma_i}\right)E_0, \tag{2.39}$$

where E_i is the magnitude of $\vec{E}_i$.

We now combine this with Eq. (2.28). This yields

$$\sum_{i=1}^{N} f_i \cdot \frac{2\sigma_E}{\sigma_E+\sigma_i}E_0 = E_0. \tag{2.40}$$

After some algebra, we obtain

$$\sum_{i=1}^{N} f_i \cdot \frac{\sigma_i - \sigma_E}{\sigma_i + \sigma_E} = 0. \tag{2.41}$$

A similar derivation for three dimensions can be found in Ref. [8] and the general result for D dimensions is

$$\sum_{i=1}^{N} f_i \cdot \frac{\sigma_i - \sigma_E}{\sigma_i + (D-1)\sigma_E} = 0. \tag{2.42}$$

This approach assumed a discrete number of puddles. One may easily change the sum to an integral to obtain the EMT used by Adam and others [1]. Now, our sample is assumed to have some conductivity that is a function of the local carrier density, n. Negative n represents regions that have holes and n follows some distribution $P(n)$. We have

$$\int_{-\infty}^{\infty} dn P(n) \frac{\sigma(n) - \sigma_E}{\sigma(n) + (D-1)\sigma_E} = 0. \tag{2.43}$$

$P(n)$ is assumed to be a Gaussian and is given by

$$P(n) = P(n, n_0, n_{\text{rms}}) = \frac{1}{\sqrt{2\pi} n_{\text{rms}}} \exp\left(-\frac{n - n_0}{\sqrt{2} n_{\text{rms}}} \right)^2. \tag{2.44}$$

Note that in order to use the EMT in the presence of magnetic fields, we only need to modify the local conductivity in each region $\sigma(n)$ with $\sigma(n, B)$.

2.1.5 Analytical two channel model result and the EMT

While the EMT result is numerical, there is one useful case where an analytical result can be expressed in notation of the EMT formalism. Consider a two channel model with charge carrier concentrations n_e and n_h. Using Eq. 2.11, $\vec{J} = \hat{\sigma}\vec{E}$ and $\hat{\rho} = \frac{1}{\hat{\sigma}}$, we express the resistivity as given below

$$\rho_{xx} = \frac{1}{n_e + n_h} \left(\frac{1 + (\mu B)^2}{1 + (\alpha \mu B)^2} \right) \tag{2.45}$$

$$\rho_{xy} = \frac{\alpha \mu B}{n_e + n_h} \left(\frac{1 + (\mu B)^2}{1 + (\alpha \mu B)^2} \right). \tag{2.46}$$

A Taylor expansion of ρ_{xx} in B gives

$$\rho_{xx}(B) = \rho_{xx}(0)[1 + (1 - \alpha^2)(\mu B)^2 + ...]. \tag{2.47}$$

The coefficient of the quadratic μB term is called A. That is $A = (1 - \alpha^2)$. We shall now express A in terms of n_0 and n_{rms} from the continuous EMT model. Note that we are ignoring the effect of spatial variation here and are using the two channel result to calculate the MR. The carrier concentrations are given by the following integrals

$$n_e = \int_0^\infty nP(n)dn \tag{2.48}$$

$$n_h = \int_{-\infty}^0 -nP(n)dn. \tag{2.49}$$

Thus, we have

$$n_e - n_h = \int_{-\infty}^\infty nP(n)dn \tag{2.50}$$

$$n_e + n_h = \int_{-\infty}^\infty |n|P(n)dn. \tag{2.51}$$

Evaluating the integrals, we can now calculate α. We define $k = n_0/n_{\text{rms}}$ and find,

$$\alpha = \frac{k\sqrt{2\pi}}{2e^{\frac{-k^2}{2}} + k\sqrt{2\pi}Erf(\frac{k}{\sqrt{2}})}. \tag{2.52}$$

Here, we have used the error function

$$Erf(x) = \frac{2}{\sqrt{\pi}} \int_0^x e^{-t^2} dt.$$

That is, the magnetoresistance coefficient A is given by

$$\begin{aligned} A =& 1 - \alpha^2 \\ =& 1 - \left(\frac{k\sqrt{2\pi}}{2e^{\frac{-k^2}{2}} + k\sqrt{2\pi}Erf(\frac{k}{\sqrt{2}})} \right)^2. \end{aligned} \tag{2.53}$$

2.2 Impurity scattering and transport

In this section we derive the transport scattering time which can be used to obtain the Boltzmann conductivity. We follow the derivation done in Chapter 13 and 16 of Ref. [31]. Firstly, we note that the discussion that follows happens for electrons in some band n, at position $\mathbf{r}$ and at some time t. We shall assume that the electrons scatter within the same band (a condition that elastic scattering will later impose anyway) and we suppress the position and time variables for ease of notation.

The probability that an electron with wave vector $\mathbf{k}$ will scatter into some phase space volume element $d\mathbf{k}'$ about $\mathbf{k}'$ in some time dt is given by

$$\frac{W_{\mathbf{k},\mathbf{k}'}\ dt d\mathbf{k}'}{(2\pi)^3}. \tag{2.54}$$

Here, $W_{\mathbf{k},\mathbf{k}'}$ depends on the scattering mechanism. Electrons are assumed to undergo a collision with a probability $dt/\tau(\mathbf{k})$. The probability of $\mathbf{k}'$ being unoccupied is merely $1 - g(\mathbf{k}')$, where the local non-equilibrium distribution function is $g(\mathbf{k})$. The transition rate must reduce by this factor and hence, we obtain

$$\frac{1}{\tau(\mathbf{k})} = \int \frac{d\mathbf{k}'}{(2\pi)^3} W_{\mathbf{k},\mathbf{k}'}[1 - g(\mathbf{k}')]. \tag{2.55}$$

The change in the local non-equilibrium distribution function due to electrons being scattered out of $\mathbf{k}$ is

$$\begin{aligned}\left(\frac{dg(\mathbf{k})}{dt}\right)_{out} &= -\frac{g(\mathbf{k})}{\tau(\mathbf{k})} \\ &= -\int \frac{d\mathbf{k}'}{(2\pi)^3} W_{\mathbf{k},\mathbf{k}'}[1 - g(\mathbf{k}')]g(\mathbf{k}).\end{aligned} \tag{2.56}$$

Similarly, we also have electrons being scattered into the volume around $\mathbf{k}$. These originally had a wave vector $\mathbf{k}'$ over which we must sum and we have

$$\left(\frac{dg(\mathbf{k})}{dt}\right)_{in} = \int \frac{d\mathbf{k}'}{(2\pi)^3}\ W_{\mathbf{k}',\mathbf{k}}[1 - g(\mathbf{k})]g(\mathbf{k}'). \tag{2.57}$$

Summing the two effects, we have

$$\left(\frac{dg(\mathbf{k})}{dt}\right)_{tot} = -\int \frac{d\mathbf{k}'}{(2\pi)^3}\left[W_{\mathbf{k},\mathbf{k}'}(1-g(\mathbf{k}'))g(\mathbf{k}) - W_{\mathbf{k}',\mathbf{k}}(1-g(\mathbf{k}))g(\mathbf{k}')\right]. \tag{2.58}$$

Note that using the relaxation time approximation for the same collisions with $g^0(\mathbf{k},\mathbf{r},t)$ being the local equilibrium distribution function, we have

$$\left(\frac{dg(\mathbf{k})}{dt}\right)_{tot} = \frac{g^0(\mathbf{k}) - g(\mathbf{k})}{\tau(\mathbf{k})}. \tag{2.59}$$

Using Fermi's Golden Rule, we can show that for elastic scattering off an impurity with a symmetric potential U and a concentration of n_{imp} impurities, we have

$$W_{\mathbf{k},\mathbf{k}'} = W_{\mathbf{k}',\mathbf{k}} = \frac{2\pi}{\hbar} n_{\text{imp}} \delta(\mathcal{E}_{\mathbf{k}} - \mathcal{E}_{\mathbf{k}'}) |\left\langle \mathbf{k} \right| U \left| \mathbf{k}' \right\rangle|^2. \tag{2.60}$$

It is also known (but we shall not derive it here) that when the energy $\mathcal{E}_{\mathbf{k}}$ only depends on magnitude k of $\mathbf{k}$, the distribution function that is a valid solution to the Boltzmann equation takes the form $g(\mathbf{k}) = g^0(\mathbf{k}) + \mathbf{a}(\mathcal{E}).\mathbf{k}$. Within the relaxation time approximation, we have (using Eq. (2.59) and Eq. (2.58))

$$\mathbf{a}(\mathcal{E}) \cdot \int \frac{d\mathbf{k}'}{(2\pi)^3}\, W_{\mathbf{k},\mathbf{k}'}(\mathbf{k}-\mathbf{k}') = \frac{1}{\tau(\mathbf{k})}\mathbf{a}(\mathcal{E}) \cdot \mathbf{k}. \tag{2.61}$$

Recalling that the magnitudes of $\mathbf{k}$ and $\mathbf{k}'$ are equal we now impose that the scattering can only depend on the angle between $\mathbf{k}$ and $\mathbf{k}'$. Hence, we only retain the $\hat{\mathbf{k}}.\mathbf{k}'$ part of $\mathbf{k}'$.

$$\frac{1}{\tau(\mathbf{k})} = \int \frac{d\mathbf{k}'}{(2\pi)^3} W_{\mathbf{k},\mathbf{k}'}(1 - \hat{\mathbf{k}} \cdot \hat{\mathbf{k}'}). \tag{2.62}$$

Substituting Eq. (2.60) and denoting θ to be the angle between $\mathbf{k}$ and $\mathbf{k}'$, we get

$$\frac{\hbar}{\tau(\mathbf{k})} = 2\pi\, n_{\text{imp}} \int \frac{d\mathbf{k}'}{(2\pi)^3} |\left\langle \mathbf{k} \right| U \left| \mathbf{k}' \right\rangle|^2 (1-\cos\theta)\delta(\mathcal{E}_{\text{k}} - \mathcal{E}_{\text{k}'}). \tag{2.63}$$

Next, we consider the semiclassical equations of motion for an electron in the absence of collisions. We have the force $\mathbf{F}(\mathbf{r}, \mathbf{k})$ due to the electric field E and the Lorentz force due to the magnetic field $\mathbf{B}$

$$\begin{aligned} \dot{\mathbf{r}} &= \mathbf{v}(\mathbf{k}) \\ \hbar\dot{\mathbf{k}} &= -e\left(\mathbf{E} + \mathbf{v} \times \mathbf{B}\right) = \mathbf{F}(\mathbf{r}, \mathbf{k}). \end{aligned} \tag{2.64}$$

Since the evolution is well defined, the solution to this tells us how the distribution function must evolve

$$g(\mathbf{r}, \mathbf{k}, t) = g\left(\mathbf{r} - \mathbf{v}(\mathbf{k})dt, \mathbf{k} - \mathbf{F}\frac{dt}{\hbar}, t - dt\right). \tag{2.65}$$

Any additional changes must be due to collisions that remove or add electrons from/to the state $(\mathbf{r}, \mathbf{k})$. Thus, we have

$$g(\mathbf{r}, \mathbf{k}, t) = g\left(\mathbf{r} - \mathbf{v}(\mathbf{k})dt, \mathbf{k} - \mathbf{F}\frac{dt}{\hbar}, t - dt\right) + \left(\frac{\partial g}{\partial t}\right)_{col}. \tag{2.66}$$

A linear order expansion now yields the Boltzmann equation

$$\left(\frac{\partial g}{\partial t}\right)_{col} = \frac{\partial g}{\partial t} + \mathbf{v} \cdot \frac{\partial}{\partial \mathbf{r}} g + \mathbf{F} \cdot \frac{1}{\hbar}\frac{\partial}{\partial \mathbf{k}} g. \tag{2.67}$$

Within the relaxation time approximation, if we consider no magnetic field (we shall add the magnetic field using the Lorentz force to the current later), static electric field $\mathbf{E}$, and uniform temperature, the solution to the Boltzmann equation is

$$g(\mathbf{k}) = g^0(\mathbf{k}) - e\mathbf{E} \cdot \mathbf{v}(\mathbf{k})\tau(\mathbf{k})\left(-\frac{\partial f}{\partial \mathcal{E}}\right). \tag{2.68}$$

Here $f(\mathcal{E})$ is the Fermi distribution at energy $\mathcal{E}$. The number of carriers can be worked out from the density of states, $\nu(\mathcal{E})$, and the probability of occupancy $g(\mathcal{E}(k))$. The current density can be worked out from the carrier concentration and the velocity $\mathbf{v}(\mathbf{k})$. We have

$$\mathbf{J} = \int d\mathcal{E}\nu(\mathcal{E})g(\mathbf{k})\mathbf{v}(\mathbf{k}). \tag{2.69}$$

We also have $\mathbf{J} = \boldsymbol{\sigma}\mathbf{E}$ and we ignore the equilibrium part of $g(\mathbf{k})$ in Eq. (2.68) since it does not contribute to the conductivity. Assuming isotropic $\boldsymbol{\sigma}$, we then obtain the diagonal conductivity in D dimensions to be [32]

$$\sigma = \frac{e^2}{D} \int d\mathcal{E} \nu(\mathcal{E}) |\mathbf{v}(\mathbf{k})|^2 \tau(\mathcal{E}(\mathbf{k})) \left(\frac{\partial f}{\partial \mathcal{E}} \right). \tag{2.70}$$

Finally, we observe that at zero temperature, the Fermi function is merely a step function and hence, its derivative is merely a delta function that picks out the Fermi energy $\mathcal{E}_F$ in Eq. (2.70). This yields the well known Einstein conductivity relation in three dimensions.

$$\sigma = \frac{e^2}{3} v_F^2 \nu(\mathcal{E}_F) \tau(\mathcal{E}_F). \tag{2.71}$$

Here, $\tau(\mathcal{E}_F)$ can be determined from Eq. (2.63)

Chapter 3

Graphene

3.1 Introduction to graphene

Graphene is a two dimensional allotrope of carbon where sp2 hybridized carbon atoms are packed in a hexagonal honeycomb pattern. Since the seminal experimental work of Novoselov and Geim [10] that isolated graphene sheets of atomic thickness, graphene has become a major research area in condensed matter physics. There is an immense amount of work that has already been done and is currently being done on graphene and we point the reader to several excellent reviews [33, 34] for further details and references. The mechanical [35], electronic [32], chemical [36] and optical [37] properties are all uniquely interesting but we shall focus only on the electronic properties that are of relevance to this chapter.

Significantly before experimental efforts to isolate graphene, P.R. Wallace used the tight binding approximation to calculate the band structure of graphene [38] and discovered several unusual properties as shown in Fig. 3.1. In particular, the existence of the so-called Dirac points where the conduction and valence band touch has been the focus of much investigation. At low energies around the Dirac points, the charge carriers behave as massless fermions and their dynamics are prescribed by the Dirac equation instead of the massive equivalent - the Schrodinger equation. The linear energy momentum relationship results in a constant density of states and a constant Fermi velocity. Additionally,

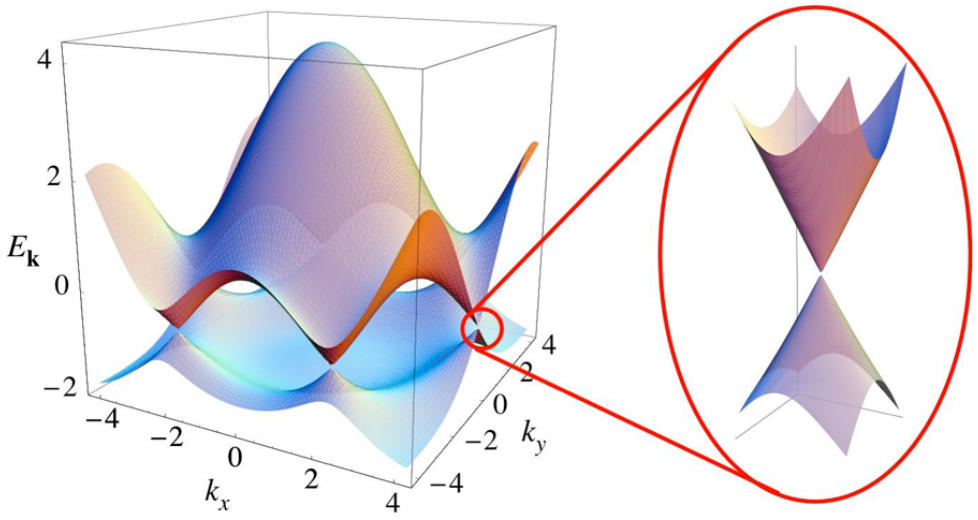

FIGURE 3.1: The band structure of graphene calculated using the tight binding method shows touching bands at the six non-equivalent points in the Brillouin zone. At low energies, the zoomed image shows the conical dispersion due to the linear energy momentum relation. This property results in the electrons behaving as massless Dirac fermions. Image from Ref. [33]

graphene shows extremely high mobilities at room temperature which have made it an excellent candidate for various technological applications.

In this work, we consider graphene on a substrate with charged impurities on the substrate. The impurities are present at some distance d from the graphene sheet and the effective fine structure constant of graphene on a particular substrate, α_{eff}, is what determines the extent to which the impurity potential causes scattering of the charge carriers. In addition to scattering, the random impurity positions also lead to a random induced carrier density across the sample i.e. macroscopic inhomogeneity. The essential idea here is that the random spatially varying impurity potential is screened through the induced carriers and hence, the induced carrier concentration is also random and spatially varying. Therefore, the use of the EMT is the required to calculate the conductivity.

3.2 Theoretical background

We shall not explicitly derive the Boltzmann conductivity of graphene here. It is well known [32] that the form $\sigma = ne\mu$ where μ is independent of carrier density is the right ansatz for the conductivity. In order to make a comparison with the experiment, we take

the zero field conductivity results and fit μ using the parameters d, n_{imp} and σ_s which are the effective distance of the charged impurities from the graphene sheet, the concentration of the charged impurities and the contribution of short range scatterers respectively.

The Boltzmann conductivity of $\sigma = ne\mu$ implied that the conductivity of graphene would be zero at the Dirac point where $n = 0$. However, actual experimental results found that this was not the case [10]. The reason for this was eventually shown to be due to disorder [32] which resulted in an effective minimum n that will be referred to as n^*. Indeed, experimental confirmation of the presence of puddles was done by STM measurements in Ref. [39] which showed that fluctuations around the Dirac point ensured that the local Fermi energy was never precisely zero. This experimental result is shown in Fig. 3.2. With this in mind, we apply the effective medium theory to graphene.

The local Boltzmann conductivity matrix in the presence of a magnetic field is given by

$$\hat{\sigma} = \begin{pmatrix} \sigma_{xx} & \sigma_{xy} \\ -\sigma_{xy} & \sigma_{xx} \end{pmatrix}. \tag{3.1}$$

In the presence of a magnetic field, these are merely

$$\sigma_{xx} = \sigma_0(n)\frac{1}{1+\mu^2B^2}\,,\ \sigma_{xy} = \sigma_0(n)\frac{\mu B}{1+\mu^2B^2}, \tag{3.2}$$

where $\sigma_0(n) = ne\mu$. We wish to find the EMT conductivity matrix

$$\hat{\sigma}^E = \begin{pmatrix} \sigma^E_{xx} & \sigma^E_{xy} \\ -\sigma^E_{xy} & \sigma^E_{xx}, \end{pmatrix}. \tag{3.3}$$

Using Eq.(2.42), with $D = 2$, we have

$$\int dn\ P[n, n_0, n_{\text{rms}}]\frac{(\hat{\sigma}(n) - \hat{\sigma}^E)}{\left(\hat{\mathbb{I}}_2 + \frac{\hat{\mathbb{I}}_2}{2\hat{\sigma}^E_{xx}}(\hat{\sigma}(n) - \hat{\sigma}^E)\right)} = 0, \tag{3.4}$$

Note that to go from Eq.(2.42) to Eq.(3.4), one needs to introduce the concept of a depolarization tensor [40]. Eq. (2.42) was done assuming scalar conductivities but when we change to a conductivity matrix, this is the appropriate generalization and implicitly

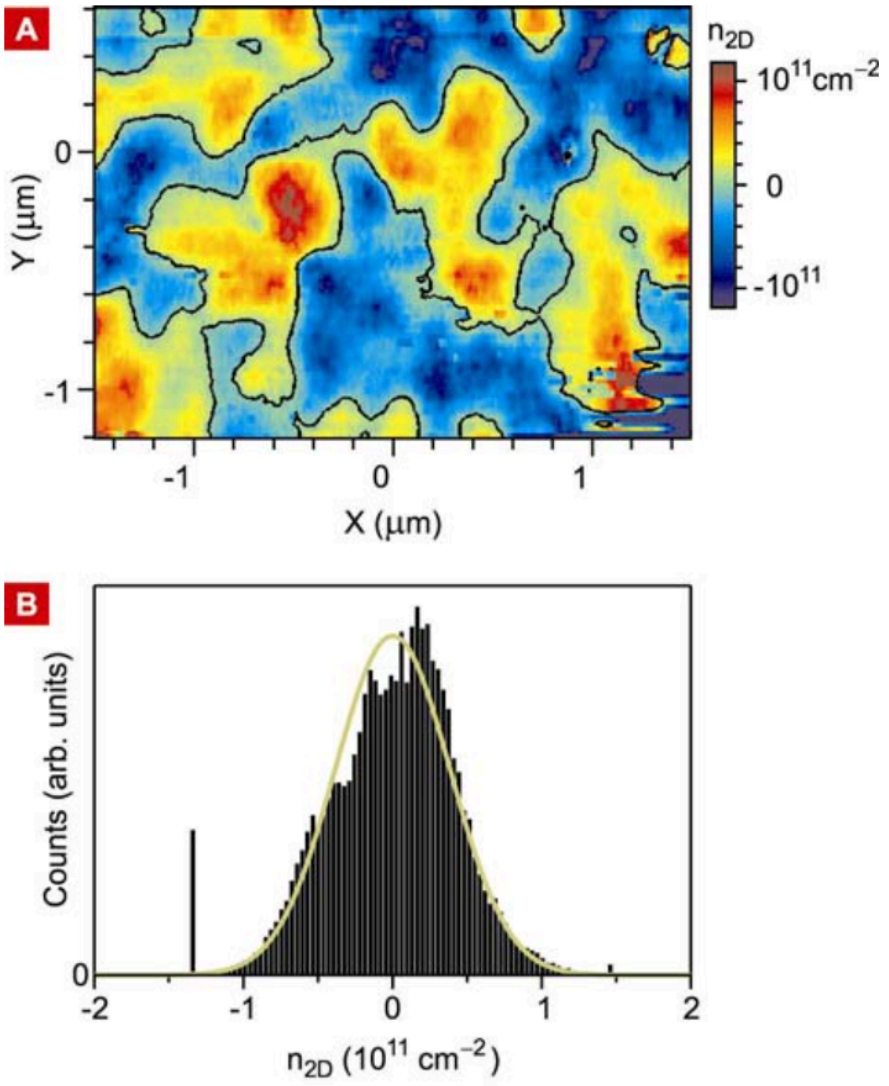

FIGURE 3.2: The first panel shows the spatially varying carrier concentrations in graphene where blue regions correspond to holes and red to electrons. Zero density regions are marked in black. The histogram in the second panel is the carrier density distribution that should be used in the EMT. Image from Ref. [39]

assumes circular puddles. Note that in the case where $\sigma_{xy} = 0$, we recover Eq. (2.42). Thus, we have from Eq. (3.2) and Eq.(3.4)

$$\int dn P[n, n_0, n_{\text{rms}}] \frac{\sigma_{xx}^2[n] - (\sigma_{xx}^{\text{EMT}})^2 + (\sigma_{xy}^{\text{EMT}} - \sigma_{xy}[n])^2}{(\sigma_{xx}^{\text{EMT}} + \sigma_{xx}[n])^2 + (\sigma_{xy}^{\text{EMT}} + \sigma_{xy}[n])^2} = 0 \tag{3.5a}$$

$$\int dnP[n, n_0, n_{\rm rms}] \frac{\sigma_{xy}[n] - \sigma_{xy}^{\rm EMT}}{(\sigma_{xx}^{\rm EMT} + \sigma_{xx}[n])^2 + (\sigma_{xy}^{\rm EMT} + \sigma_{xy}[n])^2} = 0. \tag{3.5b}$$

A simplified version of the EMT code that shows how Eq. (3.4) is solved is shown in Appendix A. The full expansion of the equations yields some important insights. The EMT equations in any dimension D consist of two equations that take the form

$$\int dnP(n, n_0, n_{\rm rms}) F\left(\sigma_{xx}, \sigma_{xy}, \sigma_{xx}^{EMT}, \sigma_{xy}^{EMT}\right) = 0, \tag{3.6}$$

where we $F(a, b, c, d)$ is a function that has terms of the same degree in both the numerator and the denominator. For example, in two dimensions, we have

$$F = \frac{\sigma_{xx}^2[n] - (\sigma_{xx}^{\rm EMT})^2 + (\sigma_{xy}^{\rm EMT} - \sigma_{xy}[n])^2}{(\sigma_{xx}^{\rm EMT} + \sigma_{xx}[n])^2 + (\sigma_{xy}^{\rm EMT} - \sigma_{xy}[n])^2}. \tag{3.7}$$

Next, we note that

$$\sigma_{xx} = \frac{ne\mu(n)}{1 + \mu(n)^2 B^2}\ ,\ \sigma_{xy} = \frac{ne\mu(n)}{1 + \mu(n)^2 B^2}\mu(n)B. \tag{3.8}$$

We also have $P[n, n_0, n_{\rm rms}] = \frac{1}{\sqrt{2\pi} n_{\rm rms}} e^{(n_0 - n_{\rm rms})^2 / 2n_{\rm rms}^2}$. Changing variables to $\tilde{x} = x/n_{\rm rms}$ for any variable x, we have the EMT equations

$$\int d\tilde{n} e^{(\tilde{n} - \tilde{n}_0)^2} F\left(\frac{\tilde{n}e\mu(\tilde{n})}{1 + \mu(n)^2 B^2}, \frac{\tilde{n}e\mu(\tilde{n})}{1 + \mu(n)^2 B^2}\mu(n)B, \tilde{\sigma}_{xx}^{EMT}, \tilde{\sigma}_{xy}^{EMT}\right) = 0, \tag{3.9}$$

Note that we are only allowed to change variables due to the zero on the right hand side and the properties of F. We cannot change n to $\tilde{n}$ for the $\mu(n)$ associated with a B term yet. However, if $\mu(n) \sim n^0$, then one may note that the solution of the two integral equations for the EMT conductivities can only result in $\tilde{\sigma}_{xx}^{EMT}$ and $\tilde{\sigma}_{xy}^{EMT}$ that are functions of $\tilde{n}_0, \mu$ and B. This also implies that the magnetoresistance is also a function of only $\tilde{n}_0, \mu$ and B.

Since μ is indeed a constant with respect to carrier density in graphene, one may rescale the magnetic field to obtain a dimensionless field $b = \mu B$. That is $MR = MR(\tilde{n}_0, b)$ which means that the the MR dependence on disorder can only be through the ratio

of n_0 and $n_{\rm rms}$. We remark in particular (since we shall use this result later), that the quadratic coefficient of MR is given by $MR = A(\mu B)^2$ and it follows that

$$A = A\left(\frac{n_0}{n_{\rm rms}}\right). \tag{3.10}$$

Finally, we need to obtain the value of $n_{\rm rms}$ in $P(n, n_0, n_{\rm rms})$. The minimum conductivity at zero magnetic field is purely a function of disorder. It corresponds to an effective carrier density n^*. The Fermi energy of graphene goes as $\mathcal{E} = \hbar v_F k_F \text{sign(n)}$ with $k_F = \sqrt{\pi|n|}$. This energy is equal to the root mean square of the potential energy due to the impurities present. We have

$$\begin{aligned} V_{\rm rms} &= \mathcal{E}^* \\ &= (\hbar v_F k^*) \\ &= \hbar v_F \sqrt{\pi n^*}. \end{aligned} \tag{3.11}$$

Finally, we wish to connect n^* with the fluctuations in carrier density $n_{\rm rms}$ that will be used in the EMT. In principle, one cannot assume that n follows a Gaussian distribution but in practice, this yields sufficiently accurate results. With $V(\mathbf{r})$ being equivalent to the local $\mathcal{E}(\mathbf{r})$ i.e. $V(\mathbf{r}) \sim \sqrt{|n(\mathbf{r})|}\text{sign(n)}$, we have

$$\begin{aligned} n_{\rm rms}^2 &= \langle n^2 \rangle - \langle n \rangle^2 \\ &= \frac{1}{\pi^2}\frac{1}{\hbar^4 v_F^4}\langle V^4 \rangle \\ &= \frac{1}{\pi^2}\frac{1}{\hbar^4 v_F^4}\int dV\ V^4 \frac{1}{\sqrt{2\pi V_{\rm rms}^2}} \exp\left(\frac{-V^2}{2V_{\rm rms}^2}\right) \\ &= 3\frac{1}{\pi^2}\frac{1}{\hbar^4 v_F^4} V_{\rm rms}^4 \\ \therefore n_{\rm rms} &= \frac{1}{\pi}\frac{1}{\hbar^2 v_F^2}\sqrt{3} V_{\rm rms}^2 = \sqrt{3} n^*. \end{aligned} \tag{3.12}$$

In the last step, we have used Eq. (3.11). The value of n^* is obtained from the fit to $\sigma_{\rm min} = n^* e \mu$, where $\sigma_{\rm min}$ is the zero field minimum conductivity observed in a graphene experiment. From here, we obtain $V_{\rm rms}$ and subsequently, $n_{\rm rms}$.

3.3 Comparison with experiment

We now apply the theory developed to experiments performed by our collaborators. Three samples of chemical vapor deposition (CVD) graphene and one sample of exfoliated graphene were used. Details regarding the experimental procedure can be found in Ref. [1] but are not relevant to the discussion here and are hence omitted. The zero field measurements yielded mobility values of 8300 cm^2/Vs, 8100 cm^2/Vs, 10700 cm^2/Vs and 18200 cm^2/Vs respectively and the conductivity is now fixed for a given carrier density. The carrier density could be varied using a back gate. Finally, the values of n^* for each sample were obtained using the minimum conductivity observed as the samples were tuned through the Dirac point using the back gate.

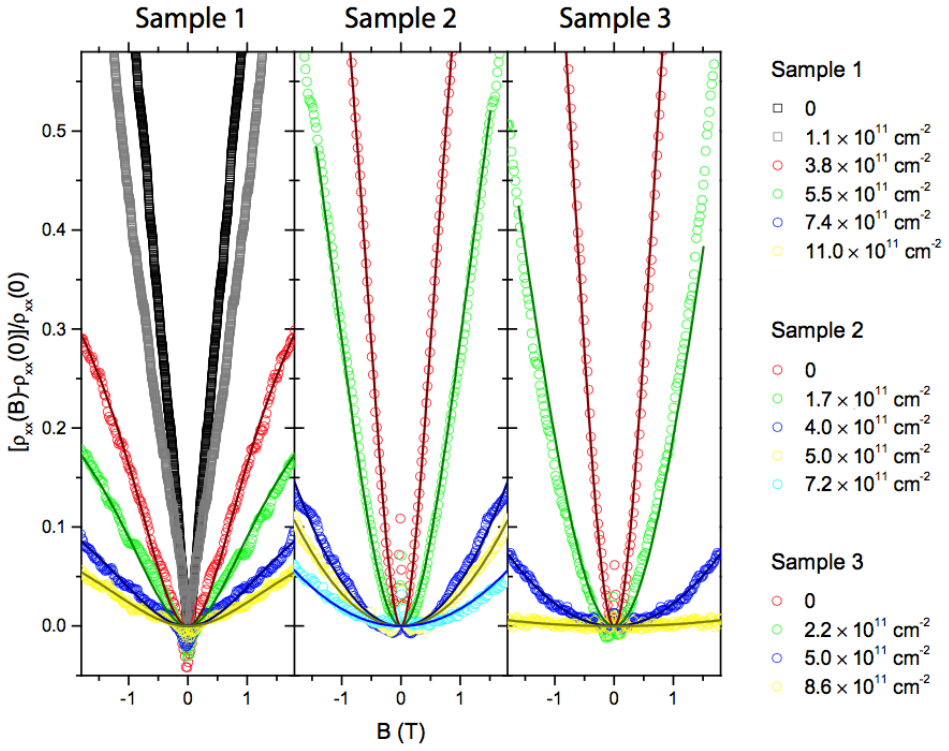

FIGURE 3.3: MR vs B curves for three different CVD samples with different gate voltages (leading to different values of n_0) are shown. The carrier densities of each dataset is given on the right. Solid fit lines using Eq. (3.13) are also shown where γ is a fit parameter. Image from Ref. [1]

We now turn to the MR results which are of interest to us. The transition from quadratic to linear MR was observed and for sufficiently low values of B, the resistivity takes the form $\rho_{xx}(B) = \rho_{xx}(0)\,[1 + A(\mu B)^2]$. The dimensionless parameter A is the quadratic

coefficient of magnetoresistance that we discussed in Eq. (3.10). The entire range of MR can be fitted to a previously known phenomenological formula given by Ref. [41]. We have

$$\rho_{xx}(B) = \rho_{xx}(0)\left[1-\gamma+\frac{\gamma}{\sqrt{1+\frac{2A(\mu B)^2}{\gamma}}}\right]^{-1}, \tag{3.13}$$

where γ is a fit parameter. This is shown along with the experimental data in Fig. 3.3.

Focusing on the low field regime, we consider the following explanations for the MR. The first is that of a two channel model where we use Eq. (2.53). This has been discussed earlier but the essential point is that it takes into account the disorder contribution due to the presence of electrons and holes that are assumed to be distributed homogeneously throughout the sample. A more primitive form of the EMT equations developed here existed in the literature due to Stroud [40]. While this also assumes two types of charge carriers, it considers macroscopic regions that consist of only electrons or only holes of fixed carrier concentration. We can cast it as a specific case of Eq. (3.5) with $P(n, n_0, n_{\rm rms})$ being a double delta function instead of a Gaussian distribution. This model is called the Area Fraction EMT since the only number that matters is the fraction of the sample area that is covered by electrons (the remainder is covered by holes).

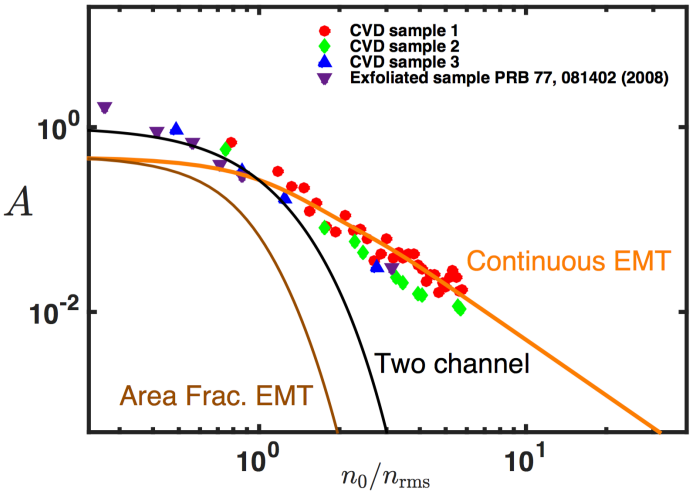

FIGURE 3.4: The quadratic coefficient is plotted against the disorder parameter $n_0/n_{\rm rms}$. It is observed that n_0 and $n_{\rm rms}$ are indeed not independent parameters. The two channel curve uses Eq. (2.53) and the Area Fraction EMT uses the model of Ref. [40]. The curve labelled "Continuous EMT" represents this work. Image from Ref. [1]

As we see in Fig. 3.4, the experimental data confirms that despite using a wide range of n_0 and $n_{\rm rms}$, only the ratio $n_0/n_{\rm rms}$ is relevant to understand the physics. Next, we note that both the two channel model and the area fraction models incorrectly predict that the MR dies away rapidly for large $n_0/n_{\rm rms}$. Only the EMT correctly predicts the persistence of disorder induced MR, even in a one channel model - a case that had been previously dismissed as equivalent to the classical Hall effect and therefore uninteresting.

Finally, we remark that Ref. [42] had solved this EMT model analytically at the Dirac point to show $A = 1/2$. Further away, the solution is numerical but is observed to follow the power law $A \sim \left(\frac{n_0}{n_{\rm rms}}\right)^{-2}$. At this point, we recollect that this is exactly what we had expected from our intuitive understanding of disorder induced MR. Indeed, Eq. 2.27, which was based on a simple two puddle model, had already described exactly the same result.

Chapter 4

Dirac Semimetals

4.1 Review of Dirac Semimetals

The spectacular success of graphene spawned the search for higher dimensional analogues with the same band structure. Broadly defined, Dirac semimetals are materials with gapless band structures and linear dispersion about the Dirac points with carrier momentum now being allowed in all three dimensions instead of two as in the case of graphene. The band structure of a Dirac semimetal including the linear dispersion at low energy is shown in Fig. 4.1.

Theoretical interest in this field only started in the early part of this decade [44–46] and experimental confirmation of the presence of Dirac points in Cd_3As_2 [47–49] TaAs [50] and TlBiSSe [51, 52] followed soon after. We refer the reader to Ref. [53] for a review on candidate materials with the requisite band structure.

Much work has been done in recent years to characterize the electronic properties of Dirac semimetals. This includes scattering due to different impurity potentials [54], quantum transport [55], thermoelectric properties [56], temperature dependent conductivity [57], quantized MR [58], diffusive transport [59] and the effects of electron-electron interactions [60]. We investigate the transport and magnetotransport properties of 3D Dirac semimetals with randomly distributed bulk Coulomb impurities. As in the case of graphene, the charged impurities are responsible for both scattering that regulates

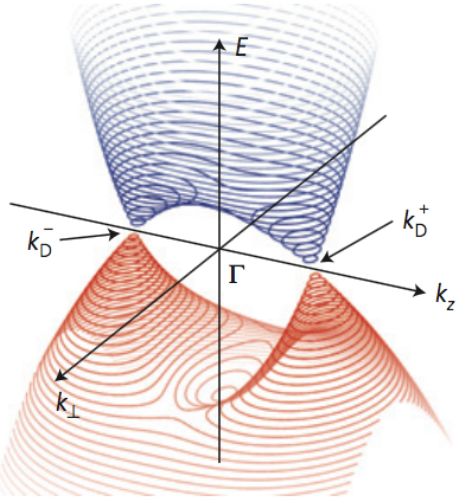

FIGURE 4.1: The figure shows a schematic of the band structure of Cd_3As_2 based on *ab initio* calculations showing two Dirac points at k_+ and k_-. Here, $k_\perp$ refers to any direction perpendicular to k_z. Reminiscent of graphene, one obtains a linear dispersion relation for low energies near the Dirac point. Image from Ref. [43].

the Boltzmann conductivity and induction of local carrier density fluctuations due to screening.

4.2 Hamiltonian and electronic properties

We start with the low energy band structure for Dirac semimetals. They are characterized by linear dispersion about the so-called Dirac points, in a manner reminiscent of graphene, except for the fact that the dispersion now occurs in three dimensions. The Hamiltonian of the system about these points is given by

$$H = \hbar \imath v_F \boldsymbol{\sigma} \cdot \boldsymbol{\partial}_{\mathbf{r}}. \tag{4.1}$$

Here $\boldsymbol{\sigma}$ is a vector of Pauli matrices, v_F is the Fermi velocity. Alternatively, this is written as

$$H = \hbar v_F k \begin{pmatrix} \cos\theta & \sin\theta e^{i\phi} \\ \sin\theta e^{-i\phi} & -\cos\theta \end{pmatrix}. \tag{4.2}$$

Here, the angles θ and ϕ represent the angles made by the $\boldsymbol{\sigma}$ vector and $\partial_{\mathbf{r}} = \mathbf{k}$ vector. Note that the case of $\theta = \pi/2$ restricts the allowed carrier momentum to two dimensions only and that is in fact the graphene Hamiltonian. Next, we can work out the eigenvalues to be $E = \pm\hbar v_F k$ and the corresponding eigenvectors to be

$$|\psi_{\pm E}\rangle = \begin{pmatrix} \sin\theta e^{i\phi} \\ \pm 1 - \cos\theta \end{pmatrix}. \tag{4.3}$$

The density of states is derived as follows. The energy dispersion is given by $\mathcal{E} = \hbar v_F k$. The quantization of $\mathbf{k}$ in a cube of length L only allows $k_x = 2\pi n_x/L$, $k_y = 2\pi n_y/L$ and $k_z = 2\pi n_z/L$. The number of allowed $\mathbf{k}$ states per unit volume in k-space is just

$$N = \frac{L^3}{(2\pi)^3}. \tag{4.4}$$

With degeneracy g, the number of available states in some sphere of radius k_F is then

$$N_s = g\frac{L^3}{(2\pi)^3}\left(\frac{4\pi k_F^3}{3}\right) = \frac{g k_F^3 L^3}{6\pi^2}. \tag{4.5}$$

The concentration of carriers per unit volume is simply $n_s = \frac{g k_F^3}{6\pi^2}$. Differentiating with respect to $\mathcal{E}$, we get the density of states

$$\nu(\mathcal{E}) = \frac{g\mathcal{E}^2}{2\pi^2\hbar^3 v_F^3}. \tag{4.6}$$

The total number of charge carriers is given by the integral of the density of states and the probability of occupancy which we obtain from the Fermi distribution. Note that all our results in this chapter are done at zero temperature and thus, we simply have a step

function at $\mathcal{E}_F$.

$$n = \int_0^{\mathcal{E}_F} d\mathcal{E}\nu(\mathcal{E}) \tag{4.7}$$
$$\mathcal{E}_F = \hbar v_F \left(\frac{6\pi^2 n}{g}\right)^{1/3}.$$

In the remainder of this chapter, we will take degeneracy $g = 4$ due to spin degeneracy and due to the presence of two Dirac points in the band structure for the materials we consider. In Eq. (4.1), we may add an impurity potential, $U(\mathbf{r} - \mathbf{R}_\mathrm{j})$ and treat it as a perturbation. $\sum_j U(\mathbf{r} - \mathbf{R}_\mathrm{j})$ is the total screened potential seen by an electron at position $\mathbf{r}$ due to charged impurities at positions $\mathbf{R}_j$. In this thesis, we consider screened Coulomb impurities.

4.3 Coulomb impurities and Boltzmann conductivity

The simplest expression for the screened Coulomb potential is the Yukawa like potential as given below, where the usual potential has an exponential screening associated with some screening radius r_s.

$$V(r) = \frac{e^2}{\kappa|\mathbf{r}|}\exp(-|\mathbf{r}|/r_s). \tag{4.8}$$

Let $\mathbf{k}$ and $\mathbf{k}'$ be the incoming and outgoing momenta of a scattered electron. Then $\mathbf{q} = \mathbf{k} - \mathbf{k}'$ is the transferred momentum. The potential corresponding to this scattering in momentum space only depends on the magnitude of $\mathbf{q}$ and is given by the Fourier transform of Eq. (4.8)

$$\begin{aligned} V(q) &= \int d\mathbf{r}\frac{e^2}{\kappa|\mathbf{r}|}\exp\left(-\frac{|\mathbf{r}|}{r_s}\right)\exp(-i\mathbf{q}.\mathbf{r}) \\ &= 2\pi\int_0^\infty dr\int_0^\pi d\theta\ r^2\sin\theta\frac{e^2}{\kappa r}\exp\left(-\frac{r}{r_s}\right)\exp(-iqr\cos\theta) \\ &= \frac{4\pi e^2}{\kappa(q^2+q_s^2)}. \end{aligned} \tag{4.9}$$

Here $q_s = \frac{1}{r_s}$. For ease of adopting different screening approximations, we rewrite our results as

$$V(q) = \frac{4\pi e^2}{\epsilon(q) q^2}, \tag{4.10}$$

The Thomas-Fermi screening approximation sets $q_s = \sqrt{\frac{2\alpha_{\text{eff}} g}{\pi}} k_F$ [61], where $\alpha_{\text{eff}} = \frac{e^2}{\hbar v_F \kappa}$ is the effective fine structure constant of the material. That is $\epsilon(q) = \kappa(1 + V_u(q)\nu(\mathcal{E}_F))$, where $V_u(q) = \frac{4\pi e^2}{\kappa q^2}$ is the unscreened potential.

A better approximation of the screening is the Random Phase Approximation (RPA). Its derivation is beyond the scope of this thesis [62] and we simply use the result. Here we have $\epsilon(q) = \kappa(1 + V(q)\tilde{\Pi}(q/2k_F)\nu(\mathcal{E}_F))$, where $\tilde{\Pi}(x)$ is the ratio of the RPA polarization function and the density of states, and is given by the sum of two components: a vacuum part $\tilde{\Pi}_V(x)$ and a finite density part $\tilde{\Pi}_M(x)$

$$\begin{aligned} \tilde{\Pi}_M(x) &= \frac{2}{3}\left[1 + \frac{1}{4x}(1 - 3x^2)\log\left|\frac{1+x}{1-x}\right| - \frac{x^2}{2}\log\left|\frac{1-x^2}{x^2}\right|\right] \\ \tilde{\Pi}_V(x) &= \frac{2x^2}{3}\log\left|\frac{\delta}{x}\right|. \end{aligned} \tag{4.11}$$

A plot of $\tilde{\Pi}(q)$ is shown in Fig 4.2.

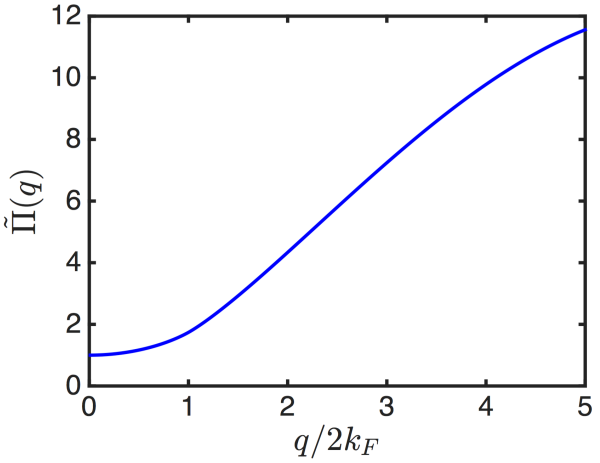

FIGURE 4.2: The ratio of the polarization function and density of states plotted with respect to q with a momentum cutoff of $\delta = 10$

One notices that the Thomas Fermi approximation essentially takes $\tilde{\Pi}(q) = 1$ i.e. the Thomas-Fermi result is merely the linearized RPA and ignores the contribution of the

vacuum part. It is only valid in the regime of $q \ll k_F$ [31] but has been sufficient in the case of graphene, for example [32]. In three dimensions, the vacuum polarization function is divergent and needs an ultraviolet momentum cutoff Δ, where in Eq (4.11), $\delta = \Delta/2k_F$. Although the transport results could, in principle, depend on the choice of this cutoff, in practice this is not the case. We use $\delta = 10$ for the results shown.

The Boltzmann transport equation is given by Eq. (2.63). We recall that the assumption of elastic scattering ensures that only intraband scattering is allowed. From Eq. (4.3), we have

$$\langle \psi_k | \psi'_k \rangle = \frac{1 + \cos\theta}{2}. \tag{4.12}$$

Thus, we have

$$\frac{\hbar}{\tau} = 4\pi\, n_{\text{imp}} \int \frac{d\mathbf{k}'}{(2\pi)^3}\, V(|\mathbf{k} - \mathbf{k}'|)^2 \frac{1 - \cos^2\theta}{4} \delta(\mathcal{E}_{\text{k}} - \mathcal{E}_{\text{k}'}). \tag{4.13}$$

The Thomas-Fermi screening approximation for $U(q)$ allows us to express the conductivity result analytically. We have, using the Einstein relation for conductivity from Eq. (2.71)

$$\sigma_{\text{TF}} = \frac{e^2 v_F^2 \tau}{3} \nu(\mathcal{E}_F). \tag{4.14}$$

Substituting Eq. (4.13), we obtain

$$\sigma_{\text{TF}} = \frac{e^2}{h} \frac{g}{12\pi^2} \frac{k_F^4}{n_{\text{imp}}\, \alpha_{\text{eff}}^2} \frac{1}{H(\sqrt{\frac{g\alpha_{\text{eff}}}{2\pi}})}, \tag{4.15}$$

where $H(z) = (z^2 + 1/2)\log(1 + z^{-2}) - 1$.

4.4 Disorder and 3D EMT equations

We now have the conductivity of a homogeneous Dirac semimetal. However, we had predicted that random Coulomb impurities would lead to the presence of macroscopic

disorder and hence fluctuations in the conductivity. STM measurements from experiments on Na_3Bi showed that this was indeed the case [63].

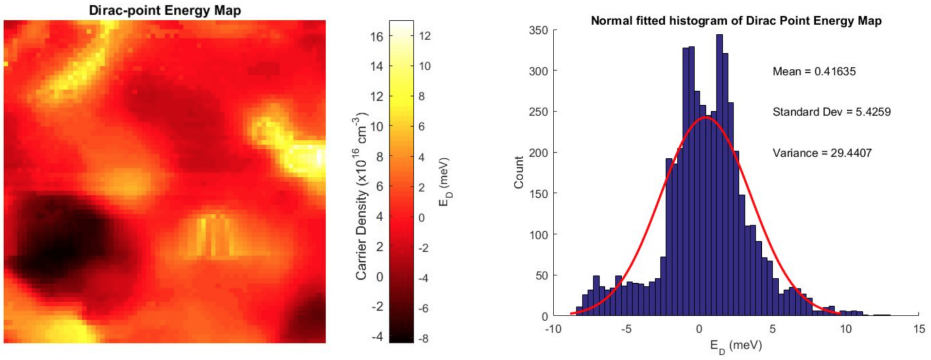

FIGURE 4.3: Experimental evidence for fluctuations in carrier density due to the presence of random impurities i.e. macroscopic disorder in Na_3Bi. Image from Ref. [63]

The self consistent ansatz for macroscopic disorder works as follows: Fluctuations in the average unscreened impurity potential lead to variations in the density of local induced carriers that screen the potential. This yields a relationship between the fluctuations in the carrier density and the fluctuations in the screened potential $V(r)$. First, we derive the fluctuations in the screened potential following the argument in Ref. [64] but in three dimensions. Let there be N_{imp} impurities located at position $\mathbf{r}_i$ with some probability $P(\mathbf{r}_i)$. If each impurity has a screened potential $V(r_i)$ at some arbitrarily defined origin (note that the potential only depends on the magnitude of $\mathbf{r_i}$), the average potential at the origin is given by $\bar{V} = \langle V \rangle$

$$\bar{V} = \int d\mathbf{r}_1 d\mathbf{r}_2 ... P(\mathbf{r}_1) P(\mathbf{r}_2) ... \sum_{i=1}^{N_{\text{imp}}} V(r_i). \tag{4.16}$$

We also note that if $P(\mathbf{r})$ is independent of $\mathbf{r}$ i.e. the impurities are isotropic and uniformly distributed on the sample, then we have $P(\mathbf{r}) = \frac{1}{L^3}$.

$$\begin{aligned}\int d\mathbf{r} P(\mathbf{r}) V(r) &= \int d\mathbf{r} P(\mathbf{r}) \int \frac{d\mathbf{q}}{(2\pi)^3}\, e^{i\mathbf{r}.\mathbf{q}} V(q) \\ &= \int d\mathbf{q}\; V(q) \frac{1}{L^3} \int \frac{d\mathbf{r}}{(2\pi)^3} e^{i\mathbf{r}.\mathbf{q}} \\ &= \frac{\tilde{V}(q=0)}{L^3}.\end{aligned} \tag{4.17}$$

Here we recall that $\tilde{V}(q)$ is the Fourier transform of the potential. We have swapped the order of integration in the second line and identified the delta function from the position integral. With the assumption that the impurities are uncorrelated, we may separate the terms of Eq. (4.16)

$$\bar{V} = n_{\text{imp}} \tilde{V}(q=0). \tag{4.18}$$

Here $n_{\text{imp}} = \frac{N\text{imp}}{L^3}$ i.e. the impurity concentration. Next we take a look at the square of the impurity potential i.e. $\langle V^2 \rangle$. We have

$$\begin{aligned}\langle V^2 \rangle &= \int d\mathbf{r}_1 d\mathbf{r}_2 ... P(\mathbf{r}_1) P(\mathbf{r}_2) ... \sum_{i,j=1}^{N_{\text{imp}}} V(r_i) V(r_j) \\ \langle V^2 \rangle - \langle V \rangle^2 &= \int d\mathbf{r}_1 d\mathbf{r}_2 ... P(\mathbf{r}_1) P(\mathbf{r}_2) ... \sum_{i=j=1}^{N_{\text{imp}}} V(r_i) V(r_j).\end{aligned} \tag{4.19}$$

Now, we consider terms of the form

$$\begin{aligned}\int d\mathbf{r} P(\mathbf{r}) V^2(\mathbf{r}) &= \int d\mathbf{r} P(\mathbf{r}) \int \frac{d\mathbf{q}}{(2\pi)^3}\, e^{i\mathbf{r}.\mathbf{q}} V(q) \int \frac{d\mathbf{q}'}{(2\pi)^3}\, e^{i\mathbf{r}.\mathbf{q}'} V(q') \\ &= \int d\mathbf{q}\; d\mathbf{q}'\; V(q) V(q') \int d\mathbf{r} P(r) e^{i(\mathbf{q}+\mathbf{q}').\mathbf{r}} \\ &= \int d\mathbf{q}\; \frac{|V(q)|^2}{L^3}.\end{aligned} \tag{4.20}$$

We have again assumed that $P(\mathbf{r}) = \frac{1}{L^3}$ and used the fact that $V(q) = V(-q)$ for Coulomb impurities. Substituting this back into Eq. (4.19) and assuming uncorrelated impurities

again, we can separate the terms to obtain

$$\langle V^2\rangle - \langle V\rangle^2 = \frac{n_{\text{imp}}}{2\pi^3}\int d\mathbf{q}\ |V(q)|^2. \tag{4.21}$$

Next, we note that $\langle V^2\rangle - \langle V\rangle^2$ defines the shift in the Fermi energy due to fluctuations of the impurity potential. The associated carrier density (which also corresponds to the minimum carrier density when the Fermi energy is at the Dirac point) is called n^* and is obtained by

$$\begin{aligned}
\mathcal{E}^{*2} &= \langle V^2\rangle - \langle V\rangle^2 \qquad (4.22)\\
(\hbar v_F k^*)^2 &= \hbar^2 v_F^2\left(\frac{6\pi^2 n^*}{g}\right)^{2/3} = \langle V^2\rangle - \langle V\rangle^2\\
\hbar^2 v_F^2\left(\frac{6\pi^2 n^*}{g}\right)^{2/3} &= \frac{n_{\text{imp}}}{2\pi^3}\int d\mathbf{q}\ |V(q)|^2.
\end{aligned}$$

Finally, we wish to connect n^* with the fluctuations in carrier density n_{rms} that will be used in the EMT. In principle, one cannot assume that n follows a Gaussian distribution but in practice, as we did in the case of graphene, this yields sufficiently accurate results. With $V \sim n^{1/3}$, we have

$$\begin{aligned}
n_{\text{rms}}^2 &= \langle n^2\rangle - \langle n\rangle^2 \qquad (4.23)\\
&= \left[\left(\frac{g}{6\pi^2}\right)^2\frac{1}{\hbar^6 v_F^6}\right]\langle V^6\rangle - \langle V^3\rangle^2\\
&= \left[\left(\frac{g}{6\pi^2}\right)^2\frac{1}{\hbar^6 v_F^6}\right]\int dV\ V^6\frac{1}{\sqrt{2\pi V_{\text{rms}}^2}}\exp\left(\frac{-V^2}{2V_{\text{rms}}^2}\right)\\
&\quad - \int dV\ V^3\frac{1}{\sqrt{2\pi V_{\text{rms}}^2}}\exp\left(\frac{-V^2}{2V_{\text{rms}}^2}\right)\\
&= 15\left[\left(\frac{g}{6\pi^2}\right)^2\frac{1}{\hbar^6 v_F^6}\right]V_{\text{rms}}^6\\
\therefore n_{\text{rms}} &= \left[\left(\frac{g}{6\pi^2}\right)\frac{1}{\hbar^3 v_F^3}\right]\sqrt{15}V_{\text{rms}}^3.
\end{aligned}$$

However, we know from Eq. (4.22) that $n^* = \left[\left(\frac{g}{6\pi^2}\right)\frac{1}{\hbar^3 v_F^3}\right]V_{\text{rms}}^3$. Thus, we have

$$n_{\text{rms}} = \sqrt{15}n^*. \tag{4.24}$$

The EMT equations for conductivity matrices are given by

$$\int dn\ P[n, n_0, n_{\text{rms}}] \frac{(\hat{\sigma}(n) - \hat{\sigma}^E)}{\left(\hat{\mathbb{I}}_2 + \frac{\hat{\mathbb{I}}_2}{3\hat{\sigma}^E_{xx}}(\hat{\sigma}(n) - \hat{\sigma}^E)\right)} = 0, \tag{4.25}$$

where we have

$$\hat{\sigma} = \begin{pmatrix} \sigma_{xx} & \sigma_{xy} \\ -\sigma_{xy} & \sigma_{xx} \end{pmatrix}, \quad \hat{\sigma}^E = \begin{pmatrix} \sigma^E_{xx} & \sigma^E_{xy} \\ -\sigma^E_{xy} & \sigma^E_{xx}, \end{pmatrix}. \tag{4.26}$$

In the presence of a magnetic field, we have

$$\sigma_{xx} = \sigma_0(n)\frac{1}{1+\mu^2 B^2}\ ,\ \sigma_{xy} = \sigma_0(n)\frac{\mu B}{1+\mu^2 B^2}, \tag{4.27}$$

where $\sigma_0(n)$ is the Boltzmann conductivity. In the case of the RPA, it is a numerical result and in the case of the Thomas-Fermi screening, it is merely Eq. (4.15). Analogous to the graphene case, the term $\frac{\mathbb{1}_2}{3\sigma^E_{xx}}$ is the depolarization tensor that assumes that the puddles are spherical. Note that in the absence of a magnetic field, $\sigma^E_{xy} = 0$ and this reduces to Eq. (2.42) with $D = 3$. Expanded out, we can get two independent EMT equations which we shall use to solve for σ^E_{xx} and σ^E_{xy}.

$$\begin{aligned} &\int dnP[n, n_0, n_{rms}] \frac{\sigma^2_{xx} + \sigma_{xx}\sigma^{EMT}_{xx} - 2(\sigma^{EMT}_{xx})^2 + (\sigma_{xy} - \sigma^{EMT}_{xy})^2}{(\sigma_{xx} + 2\sigma^{EMT}_{xx})^2 + (\sigma_{xy} - \sigma^{EMT}_{xy})^2} = 0 \\ &\int dnP[n, n_0, n_{rms}] \frac{\sigma^{EMT}_{xx}(\sigma_{xy} - \sigma^{EMT}_{xy})}{(\sigma_{xx} + 2\sigma^{EMT}_{xx})^2 + (\sigma_{xy} - \sigma^{EMT}_{xy})^2} = 0. \end{aligned} \tag{4.28}$$

4.5 Results

Having understood the theory, we now compare it with some results in the literature. We define the case of $n \gg n_{\text{rms}}$ to be the homogeneous regime where the EMT may be applied but gives very similar results to the Boltzmann conductivity and $n \ll n_{\text{rms}}$ where the EMT predicts significantly different behavior from the the Boltzmann conductivity (which predicts $\sigma \to 0$ as $n \to 0$). We first show that our RPA Boltzmann expression is correct and that the EMT indeed makes no difference in the homogeneous regime. Fig. 4.4 shows good agreement between our red curve and the blue curve of Ref. [57] at

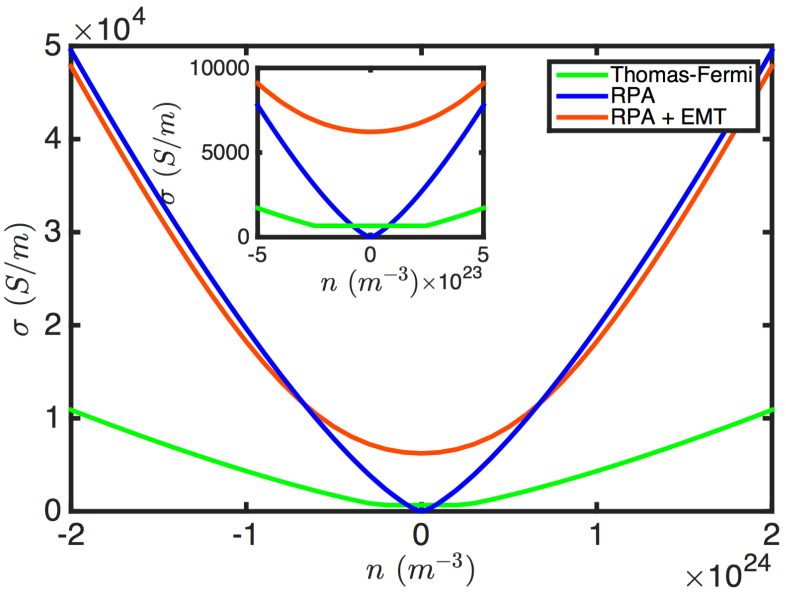

FIGURE 4.4: The blue curve shows the RPA-Boltzmann conductivity derived earlier and in Ref. [57] while the green curve shows the Thomas Fermi conductivity with a floor value as derived in Ref. [61]. The red curve shows our result of the RPA Boltzmann conductivity in conjunction with the EMT. The Thomas-Fermi conductivity is significantly different from the RPA conductivity at high n showing it is necessary to use the RPA approximation for Dirac semimetals. The EMT predicts a minimum conductivity close to the Dirac point and reproduces the Boltzmann result of $\sigma \sim n^{4/3}/n_{\rm imp}$ for large n. In order to compare with the results of Ref. [57], we follow their parameters for this figure and use $\alpha_{\rm eff} = 1.2$, $g = 2$ and $n_{\rm imp} = 10^{24} m^{-3}$ and $\tilde{\Pi}_V = 0$. The inset shows a close-up at low carrier densities near the Dirac point.

high n where $\sigma \sim n^{4/3}/n_{\rm imp}$. We note that $\tilde{\Pi}_V = 0$ was imposed by Ref. [57] and we therefore also adopt that only for this comparison. All later results use Equation. (4.11) with $\delta = 10$.

Another interesting comparison to be made is with the work of Brian Skinner in Ref. [61] which is the green curve of Fig. 4.4. Conductivity is calculated in the Thomas Fermi approximation in this case and the poor agreement at high carrier density shows that it is necessary in the case of Dirac semimetals to use the RPA approximation for screening (unlike in graphene where the two different screening approximations show a fortuitous agreement). Ref. [61] does explore the concept of a minimum conductivity. In Equation. (4.22), when we use the Thomas-Fermi screening for $U(\mathbf{q})$ on the RHS, we obtain

an analytical expression, namely

$$n^* = \sqrt{\frac{g\alpha_{\text{eff}}^3}{18\pi}} n_{\text{imp}} \tag{4.29}$$

The green curve simply imposes a floor on the conductivity corresponding to this value of n^*. Clearly, the Thomas-Fermi approximation as well as the crude floor do not accurately model the smooth transition of the conductivity from the homogeneous to the inhomogeneous regime. Furthermore, the minimum conductivity as well as the conductivity in the homogeneous regime are inaccurate compared to the RPA-EMT result.

Next, we look at some of the experimental results in the literature. Ref. [27] performs conductivity and MR experiments on TlBiSSe. The material is characterized by $v_F = 1.6 \times 10^5$ ms^{-1}, $\alpha_{\text{eff}} = 0.684$ and $g = 4$. An experimental mystery that was posited in this work was why the mobility appeared to decrease with increasing carrier density despite that fact that $\mu \sim n^{1/3}$ in the Dirac semimetal theory. We propose two possible explanations to resolve this mystery. In order to make connection with the experimental data, we define the following quantities in line with how they were calculated by Ref. [27]

$$\mu_{\text{exp}} = \lim_{B\to 0} \frac{\sigma_{\text{xy}}(B)}{B\sigma_{\text{xx}}(B)}\,,\; n_{\text{exp}} = \frac{\sigma_{\text{xx}}(B=0)}{\mu_{\text{exp}} e}. \tag{4.30}$$

Fig. 4.5 shows three theory curves in conjunction with the experimental data: The first is the naive approach where n_{imp} is fixed and the mobility is calculated using the RPA Boltzmann theory. The EMT is optional here since the value of n_{imp} that quantitatively fits the data puts us in the homogeneous regime. This is shown in the blue curve and clearly, it shows the opposite trend to the experimental data points. We therefore propose two alternatives, one in the homogeneous regime and another in the inhomogeneous regime.

The green curve assumes that the experiments are in the homogeneous regime but that the carrier density increases with increasing impurity concentration due to doping by the charged impurities, as done in a different context by Ref. [65]. That is, the average impurity potential $\bar{V} = n_{\text{imp}} U(\mathbf{q} = 0, n^*)$ is associated with the Fermi energy and therefore with the induced carrier density. We obtain $n_0 \approx 4\, n_{\text{imp}}$ and thus, the impurity concentration is no longer independent of the carrier density. With this assumption, we note

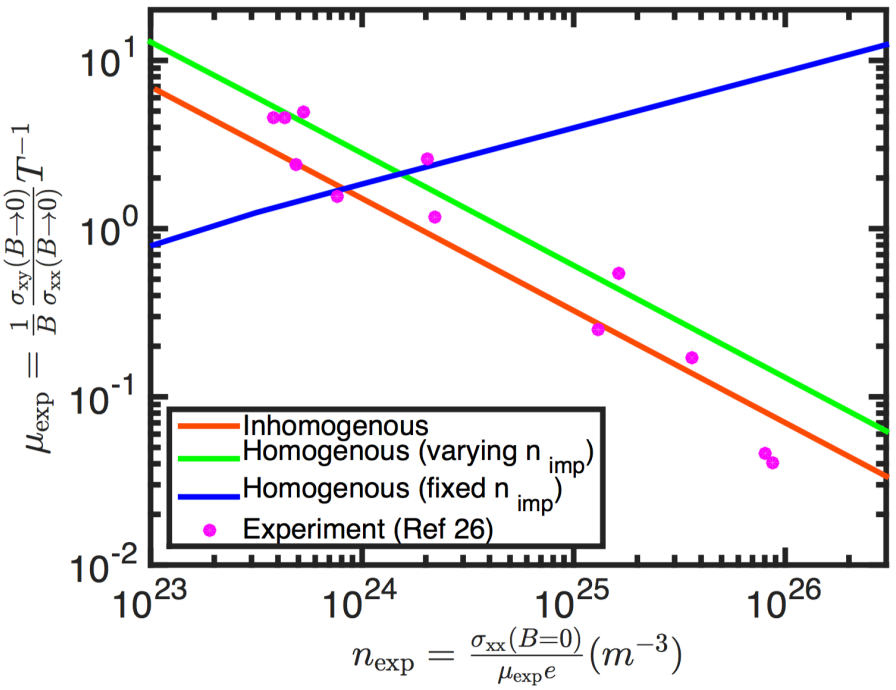

FIGURE 4.5: The experimentally calculated mobility of TlBiSSe was puzzling as it showed a decrease in experimental mobility, $\mu_{\rm exp}$, with increasing experimental carrier density $n_{\rm exp}$, which shows the opposite trend compared to the Boltzmann conductivity theory with constant $n_{\rm imp}$ (blue curve). We propose two resolutions to this experimental "mystery": The first possibility is that the experiments are in the inhomogeneous regime where $n_{\rm exp} \ll n_{\rm rms}$ and is illustrated by the red curve which uses a single fit parameter. The other possibility is that the experiments are in the homogeneous regime where $n_{\rm exp} \gg n_{\rm rms}$, but with the charged impurities also responsible for doping. Here $n_{\rm exp} = n_0 \approx 4\ n_{\rm imp}$ and the result is shown by the green curve.

that there is excellent agreement between the green theory curve and the experimental data. The correct trend of $\mu_{\rm exp} \sim n^{-2/3}$ is obtained since

$$\begin{aligned} \mu &= \frac{\sigma}{ne} \\ &\sim \frac{n^{4/3}}{n_{\rm imp} ne} \\ &\sim n^{-2/3}. \end{aligned} \tag{4.31}$$

An alternative explanation of the mobility trend is that the sample is in the inhomogeneous regime. For this set of data, we set $n_{\rm imp} = 10^{22} m^{-3}$ to $n_{\rm imp} = 10^{26} m^{-3}$ and

$n = n^*$. This yields $n_{\text{exp}} \sim 10^{23}$ to $n_{\text{exp}} \sim 10^{26}$, matching the observed experimental carrier density measurements. The μ_{exp} calculated in this way also follows $\mu_{\text{exp}} = Cn^{-2/3}$, where $C = 30$ is a fit parameter used. There are several ways to explain the value of C, including correlations among the impurity positions and the presence of non-charged scattering impurities [66, 67] but we shall not explore these in more detail in this work.

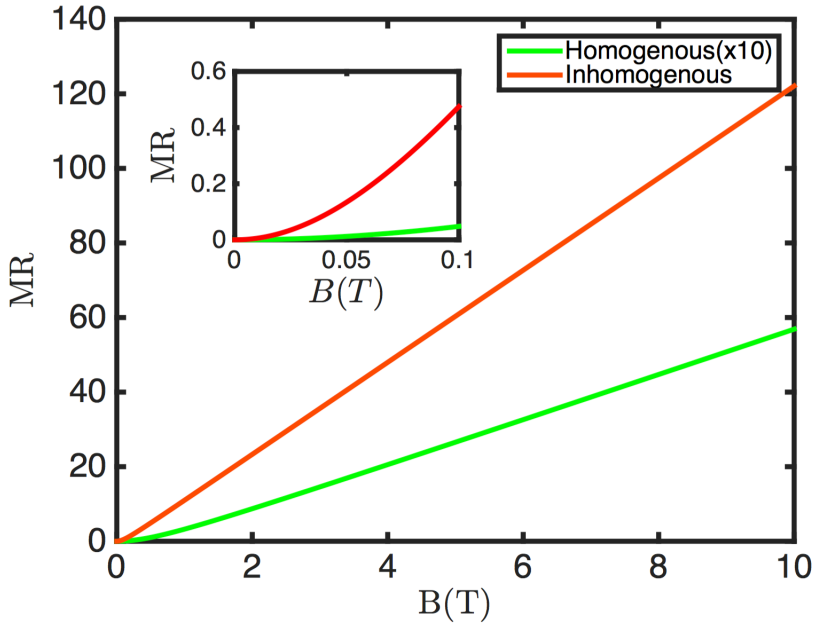

FIGURE 4.6: Magnetoresistance is shown to be a simple distinguishing mechanism between the homogeneous and inhomogeneous regimes. We consider the case of $n = 10^{23}m^{-3}$ and $n_{\text{imp}} = 2.5 \times 10^{22}m^{-3}$ for the homogeneous green curve and $n = n^* = 10^{20}m^{-3}$ and $n_{\text{imp}} = 10^{22}m^{-3}$ for the inhomogeneous red curve. Both of these would have very similar $\mu_{\text{exp}} \approx 10T^{-1}$ and $n_{\text{exp}} \approx 10^{23}m^{-3}$ at zero magnetic field making them indistinguishable. However, the MR of the inhomogeneous case is over an order of magnitude higher (note that the homogeneous result is scaled by a factor of 10 in this figure). We also obtain the quadratic to linear transition at low fields, as shown in the inset.

The question that would be foremost in the reader's mind is how we can distinguish between these two very different scenarios that both yield the same experimental mobility and carrier density measurements. The answer is to look at the magnetoresistance in the two regimes. As one may suspect by this point, the homogeneous regime would show very small MR in comparison to the inhomogeneous regime. Indeed, we pick two values that correspond to nearly the same point in Fig. 4.5, namely $(n = n^* = 10^{20}m^{-3}, n_{\text{imp}} = 10^{22}m^{-3})$ which is in the inhomogeneous regime and $(n = 10^{23}, n_{\text{imp}} = 2.5 \times 10^{22}m^{-3})$, which is in the homogeneous regime. We check the MR for $B = 0 - 10T$ and plot them

in Fig. 4.6. The inhomogeneous MR is over an order of magnitude larger (note that the homogeneous MR is scaled up by a factor of 10 in that figure) and agrees much better with the MR value that was seen in Ref. [27].

Note that $MR > 10$ can easily be achieved in this regime even with moderate values of magnetic field and we see that for technological applications involving MR, the simple solution to obtain more MR by making the samples dirtier remains true in Dirac semimetals. We also obtain the expected quadratic to linear transition in both the homogeneous and the inhomogeneous regime, which is also seen in experiments by Ref. [27]. Based on the magnitude of the MR, we conclude that those samples were likely in the inhomogeneous regime.

In summary, we have shown that our transport theory correctly matches previous theoretical work and is also able to qualitatively and quantitatively explain experimental transport results. Furthermore, we show that in cases where transport measurements cannot distinguish between the homogeneous and inhomogeneous regimes, magnetoresistance is a suitable candidate that is able to show distinguishable experimental results.

Chapter 5

Universality of disorder induced MR

We have seen two examples of how the EMT can be used to predict conductivity in the presence of magnetic fields in disordered systems. Crucially, the zero field conductivity in systems such as graphene and Weyl semimetals were sufficient to fix the parameters of the EMT and thus, the magnetoresistance was both qualitatively and quantitatively predicted by the EMT. In this chapter, we investigate an alternative model, the Random Resistor Network, developed by Parish and Littlewood [9] that has been widely used in the literature to explain disorder induced MR. We show that the two models belong to the same universality class and that their results can be mapped onto one another.

5.1 The Random Resistor Network (RRN)

The RRN model of Ref. [9] consists of a network of discrete four-terminal resistors, where the random resistivity of each unit $\rho = \frac{1}{ne\mu}$, where n is the carrier density and μ is the mobility. We consider the case where the random parameter that is drawn from a Gaussian distribution is n. The magnetic field is perpendicular to the RRN sheet. This is shown schematically in Fig. 5.1.

There are two types of RRN models in the literature, which we refer to as the fixed boundary RRN [9] and the periodic boundary RRN [68]. The fixed boundary condition imposes that the voltage drop across the sample be fixed and that the total current be conserved ($\sum_i I_i^L = \sum_i I_i^R$). The periodic boundary condition treats the sample as a tile

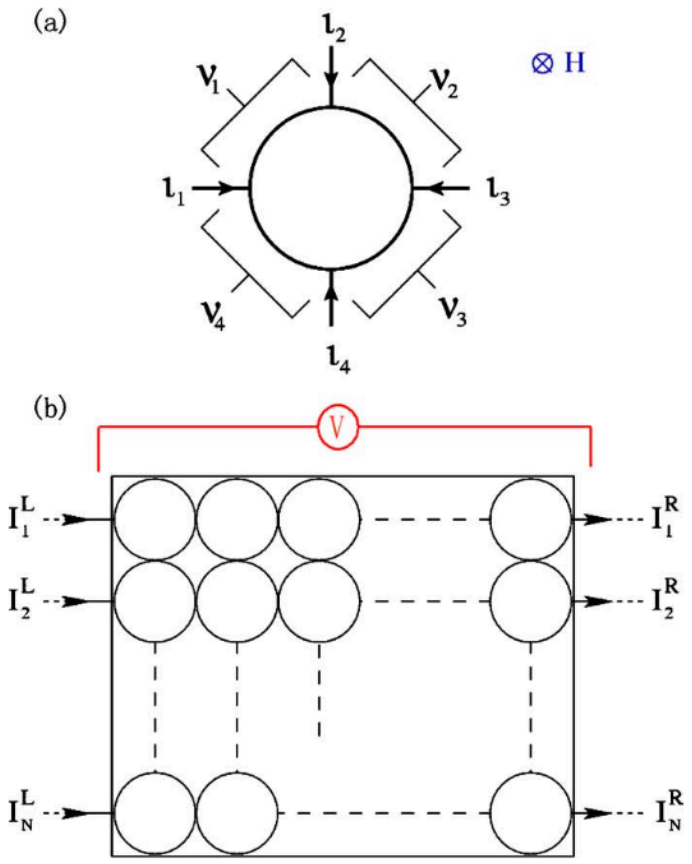

FIGURE 5.1: The schematic of the random resistor network is shown where the carrier concentration n of each resistor is randomly drawn from a Gaussian distribution. The magnetic field here points out of the plane of the page. Image from Ref. [68]

that repeats infinitely and requires the additional restriction that the current along each row is fixed ($I_i^L = I_i^R$).

We first start with the fixed boundary case. Ref [9] found that this boundary condition created an interesting edge effect even at zero disorder which resulted in MR. In fact, if $N \times N$ is the size of the RRN network, the MR curves were super-linear in the case of even N and sublinear in the case of odd N. In the limit of $N \to \infty$, the MR curve becomes quadratic to linear. To verify that we have correctly modelled the RRN, we compare our results with the results of Ref. [9] in Fig. 5.2 and find excellent agreement.

Naturally, the result that there is MR even with no disorder is clearly an artefact of these boundary conditions and does not manifest itself in the materials that we seek to model. Hence, an alternative set of boundary conditions, namely the periodic boundary

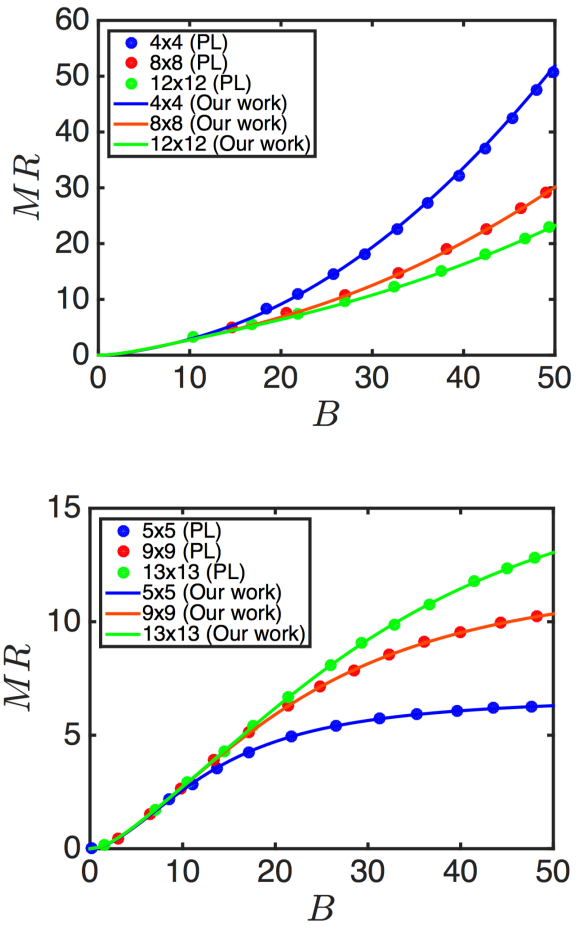

FIGURE 5.2: For an N× N RRN with zero disorder and fixed boundary conditions, even N results in MR curves that are superlinear and odd N results in MR curves that are sublinear. Our RRN model is able to correctly capture this effect and demonstrates that we have reproduced Ref. [9]. Image from Ref. [4]

conditions were then proposed by the same author and these do produce zero MR at zero disorder. Hence, we shall be using the RRN with periodic boundary conditions to compare with the EMT. Our code is attached in Appendix B. As before, the Gaussian distribution that the random value of n is drawn from is assumed to have a width n_{rms} and is centered around some value n_0. We had earlier shown that all the coefficients in the Taylor expansion of MR were functions of only one parameter and this was the ratio of the carrier density to the fluctuations in the carrier density i.e. $\frac{n_0}{n_{\text{rms}}}$. In fact, it can be numerically verified that the MR for the RRN behaves in the same way once we have fixed μ to be independent of carrier density.

The EMT and the RRN are ostensibly similar at first glance - both depend on a single parameter $\eta = \frac{n_0}{n_{\text{rms}}}$, both produce quadratic to linear MR curves and both have MR that increases with increasing disorder. The next section will investigate these features more carefully.

5.2 Comparison with the EMT

We first note that the quadratic to linear transition can be schematically represented by Fig. 5.3. We define B_q, B_c and B_l as those magnitudes of the magnetic field for which we have $MR \sim B^2$, $MR \sim B^{1.5}$ and $MR \sim B^1$ respectively. Ideally, we wish to do this comparison with as large a network size as computationally possible. We chose a 40 by 40 RRN which was sufficient to reduce the even odd effects in the fixed boundary case to negligible levels. Since the RRN is two dimensional, we compare it with the two dimensional EMT. One may envision higher dimensional RRNs of $2 \times D$ terminal resistors which could be appropriately compared against a D dimensional EMT model.

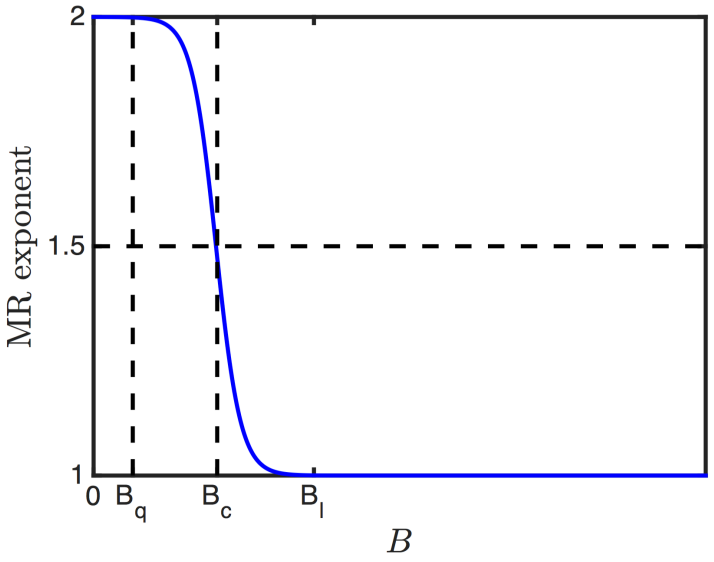

FIGURE 5.3: Definitions for B_q, B_c and B_l which are the magnitudes of the magnetic field for which the MR vs B follows a power law with exponents 2, 1.5 and 1 respectively. The tolerance that we use for our calculations when defining these quantities is 0.001.

Next, we scale the MR vs B curves by B_q along the x-axis and $MR(B_q)$ along the y axis. The tolerance used for B_q in our numerics is 0.001. We recall our previous notation

where the quadratic coefficient of MR was denoted by A. That is, $MR = A(\mu B)^2$. For simplicity, we set μ to unity since the scaling of B takes this into account anyway. Thus, our scaling has the effect of making the quadratic part of all the curves follow the line $y = x^2$ from $(0, 0)$ to $(1, 1)$. Note that scaling by $MR(B_q)$ is the same as setting $A = 1$. After this point, we know that the curves must eventually become linear and this allows us to draw a mathematical window of all allowed curves. The upper bound of the window is merely the continuation of the curve $y = x^2$ while the lower bound is the tangent drawn at $(1, 1)$ to our quadratic curve. This is given by $y = 2x - 1$. We emphasize that any curve that follows the schematic of Fig. 5.3 must lie within this window but there is no restriction beyond that.

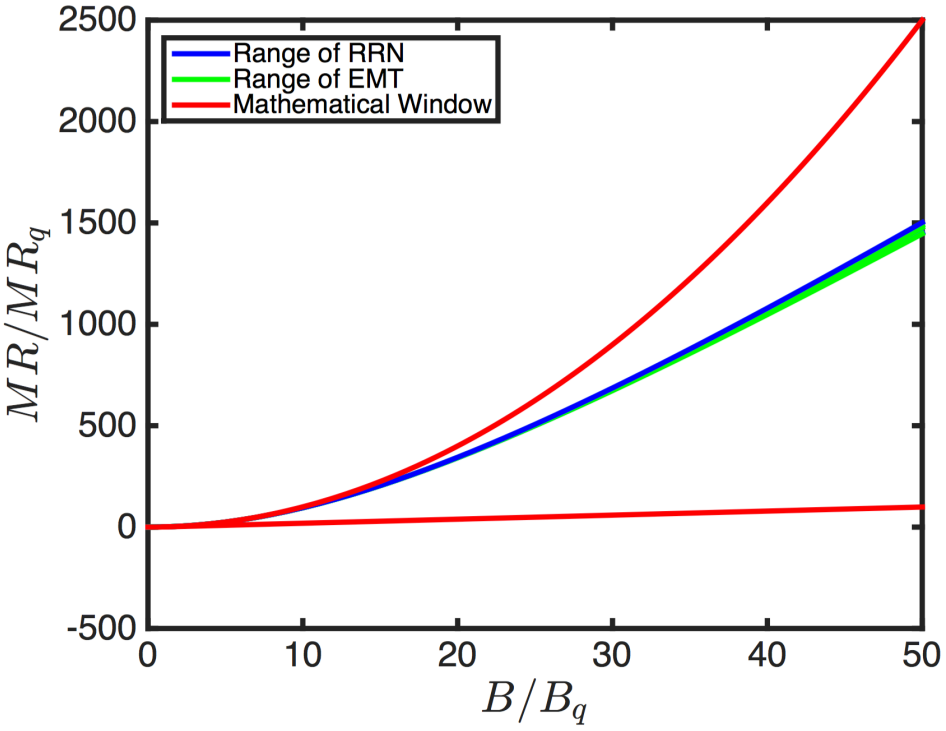

FIGURE 5.4: Collapse of disorder models onto a universal curve (up to numerical errors) when the x and y axes are scaled by B_q and MR(B_q) respectively. Note that the disorder parameter η covers a range spanning two orders of magnitude from 0.1 to 10. The mathematical window shows where all possible quadratic to linear curves may lie. Image from Ref. [4]

Astonishingly, this scaling collapses all the RRN and EMT curves with different η onto the same curve. We remark here that the collapse is not perfect due to numerical errors that arise ultimately from the tolerance of choosing B_q. Analytical approaches to find MR from either the RRN or the EMT do not exist. However, this collapse onto a small part

of the allowed phase space demonstrates convincingly that the two models belong to the same universality class. The collapse shows that any MR curve from either model can be represented by two numbers - the quadratic coefficient A and B_q. Expressed differently, we have shown that any MR vs B curve of either the RRN or the EMT model can be generated from the universal collapsed curve by simply scaling it by B_q along the x axis and the quadratic coefficient A along the y axis.

We have also verified that in the case of the RRN, for large η, the quadratic coefficient again follows $A \sim \eta^{-2}$ which is the same as in the case of the EMT, confirming that the two models do belong to the same universality class.

5.3 Experimental use

In the case of the EMT, the parameter η has a clear physical meaning since the EMT uses the Boltzmann conductivity as its input. In contrast, when we consider the RRN, the model parameter η may have no correspondence with the actual disorder in the sample being studied. That is, the RRN uses random resistance values which may have no correspondence with the resistivity distribution of the actual sample being studied. Previous experiments that have been explained with the RRN are in this sense incomplete. The MR vs B curves yield a certain η parameter but this only has meaning within the RRN model and yields no further information. Similarly, the actual disorder parameter of the sample must be "converted" into the RRN η before the magnetoresistance can be predicted. The mapping between the EMT and the RRN shows us the way to make this "conversion".

Since we are able to collapse the two curves onto the single universal curve, we now investigate the scaling that we have done which carries all the information about comparing between RRN and EMT models for a given η. In particular, we examine the quadratic coefficient A as a function of η in Fig. 5.5. For large η which corresponds to a clean system, the qualitative behavior is the same i.e. $A \sim \eta^{-2}$ but the two models show quantitatively different A values. At low η, both A curves asymptotically reach a constant value but again there are large quantitative differences.

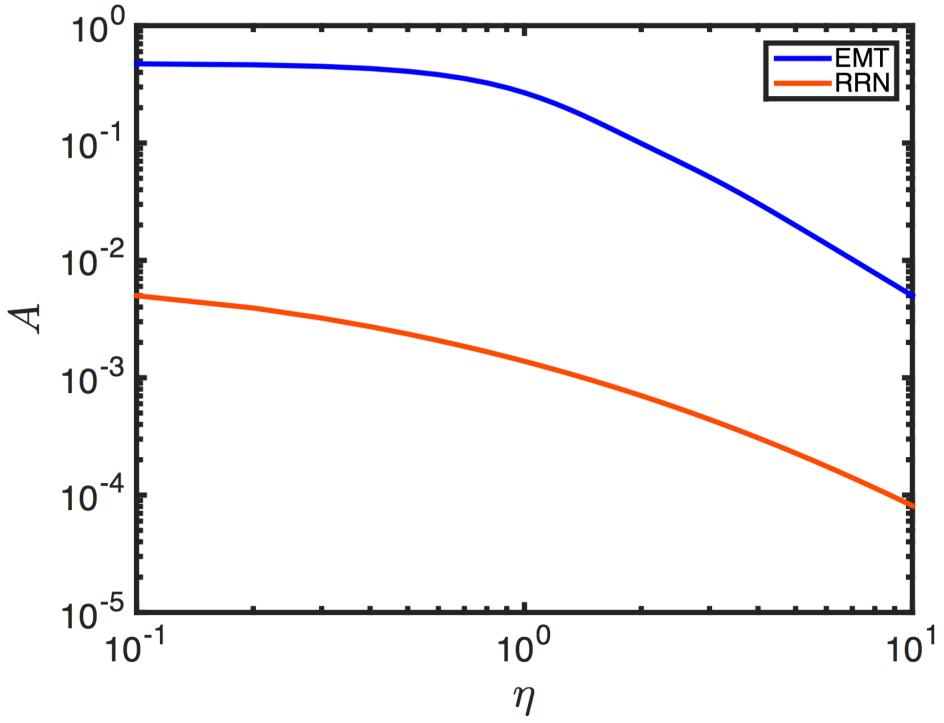

FIGURE 5.5: For a given disorder parameter η, we see quantitative differences in the A values obtained for the RRN and EMT. Qualitatively, we remark that both models obey $A \sim \eta^{-2}$ for high η and reach an asymptotic value for low η. This plot allows us to convert the disorder parameter of the RRN to the physically meaningful disorder parameter of the EMT. Image from Ref. [4]

For an experimentalist, the task is now simple. Any previous experiment that was found to conform with the RRN model can be explained using the EMT using the low field MR (low field refers to fields less than B_q) that measures A. The EMT model's η can be used to estimate other physically relevant quantities (such as the minimum conductivity) that could not be done previously. We remark that low field MR measurements are also more practical since they ensure that even in the case of low μ values in the real system, the magnetic field B required to probe this regime is still accessible.

Chapter 6

Conclusion

6.1 Summary

In this thesis, we have presented multiple interesting research problems in condensed matter physics and taken several small steps forward in many of them. We started off with a thorough understanding of semiclassical magnetoresistance and the various disorder mechanisms by which it occurs. With this intuitive picture in mind, we have adapted and developed the Effective Medium Theory in order to quantitatively characterize the effects of such disorder.

The next part was to derive the Boltzmann conductivity and use it in materials such as graphene and Dirac semimetals in the presence of randomly distributed Coulomb impurities. We noted that different screening approximations could be used and using the more correct RPA screening was necessary in the case of Dirac semimetals. The idea that macroscopic disorder was the dominant mechanism that influenced the conductivity and magnetoresistance was proposed and experimental evidence for the same was supplied. Prior results in the literature used the Area Fraction EMT or the two channel model, neither of which predicted MR away from the Dirac point. The combination of the full EMT and the correct input Boltzmann conductivity gave us good agreement with experiments, both in the case of graphene and in the case of Dirac semimetals. In the case of graphene, this model was able to correctly explain MR that persisted far away from the Dirac point and dispelled the prevalent incorrect notion that disordered one channel

MR should be zero. We also noted the use of magnetoresistance as a distinguishing mechanism between the inhomogeneous regime and the homogeneous regime, even when the zero field conductivities were very similar.

Finally, we moved on to universality. While the EMT is more physically motivated, a significant number of experiments have been described using the RRN. Our work shows that a simple scaling collapses all the magnetoresistance curves onto a single curve i.e. the two models belong to the same universality class. We also showed how one can interpret the experiments described by the RRN and translate them into the EMT picture where the disorder parameter has a clear physical meaning. Future experimentalists may generate quantitative MR curves using just two parameters that can be obtained from zero field measurements. This completes the story of how to theoretically describe disorder induced semi-classical magnetoresistance.

6.2 Future work

As is typically the case in such a broad field, there is no end to future research directions that stem from the work done so far. Here, I propose two possibilities that are of relevance and immediate interest.

The first goal that remains to be completed is the scaling of experimental data in the same way the two MR theory curves. Fitting experiments onto the same single curve after scaling ensures that a wide range of MR experiments performed on very different materials all obey the same universal model. This would then allow experimentalists to predict various parameters that depend on disorder such as the minimum conductivity based on their MR results. Conversely, the low field MR can be predicted using a single parameter η, a result that we had already shown in graphene. In fact, the entire MR curve can be predicted using just one more number, namely B_q.

A second area of research that this author is interested in is the surface states of Weyl semimetals. As discussed in Ref. [69], the breaking of certain symmetries splits the three dimensional Dirac points into two Weyl points with opposite chirality. In such cases, the surface states of Weyl semimetals show very interesting behavior with the presence of the so called Fermi arcs [50]. The edge currents are also topologically protected from

impurities and there is a large amount of research directed towards manipulating these topological properties using electrical and magnetic fields. These would allow one, in principle, to build topological transistors that would be more efficient than conventional transistors. In addition, these edge modes, by virtue of their dissipation free nature, have been suggested as possible platforms to implement quantum computation.

Appendix A

Sample EMT code

Here we show a sample of the EMT code that outputs the conductivity matrix elements for a given average carrier density n_0, width of the Gaussian n_{rms} and magnetic field B. This code finds numerically the solution to the two dimensional EMT equation. The solution is reached by iteratively refining the guess for the EMT conductivity until the error is less than a specified tolerance.

```
function [sigmaxxemt, sigmaxyemt] = sigmaemtBsimplesc(n, nrms, B, nshift)

mu=1;

if (nargin < 5) || isempty(nshift), nshift = 0; end

sigmaxx = @(nn, BB) sigmasimple(nn, mu, nshift) ./ (1 + (mu * BB) .^ 2);
sigmaxy = @(nn, BB) -sign(nn-nshift).*mu * BB .* sigmaxx(nn, BB);

denom = @(z, BB, y) (sigmaxx(z * nrms, BB) + y(1)) .^ 2 + (sigmaxy(z * nrms, BB) - y(2))
     .^ 2;

%For sc iteration
numiter1 = @(z, BB, y) (sigmaxx(z * nrms, BB) .^ 2 + (sigmaxy(z * nrms, BB) - y(2)) .^
    2) ./ denom (z, BB, y);
numiter2 = @(z, BB, y) sigmaxy(z * nrms, BB) ./ denom (z, BB, y);

%Integration limit
f = 5.3; %Optimized

%Gaussian distribution
p = @(z, z0) exp(-1 * ((z - z0) .^ 2) / 2) / ((sqrt(2 * pi)) * nrms);

numiterp1 = @(z, z0, BB, y) p(z, z0) .* numiter1(z, BB, y);
numiterp2 = @(z, z0, BB, y) p(z, z0) .* numiter2(z, BB, y);
```

```
denomp = @(z, z0, BB, y) p(z, z0) ./ denom(z, BB, y);

fnum1 = @(z0, BB, y) integral(@(z) numiterp1(z, z0, BB, y), z0 - f, z0 + f);
fnum2 = @(z0, BB, y) integral(@(z) numiterp2(z, z0, BB, y), z0 - f, z0 + f);
fdenom = @(z0, BB, y) integral(@(z) denomp(z, z0, BB, y), z0 - f, z0 + f);

fiter1 = @(z0, BB, y) fnum1(z0, BB, y) / fdenom(z0, BB, y);
fiter2 = @(z0, BB, y) fnum2(z0, BB, y) / fdenom(z0, BB, y);

%First guess based on sigma_min
nstar = nrms / sqrt(3);
sigmamin = sigmasimple(nstar, mu, nshift);
fsigmacrudexx = @(nn, BB) (sigmasimple(nn, mu, nshift) .* (abs(nn - nshift) > nstar) +
    sigmamin * (abs(nn - nshift) <= nstar)) ./ (1 + (mu * BB) .^ 2);

%Self consistent function
    function [Ansx, Ansy] = solve(ng, BB, delta)
        %Guess
        y0 = Inf;
        y1 = [fsigmacrudexx(ng, BB); sigmaxy(ng, BB)];

        %Solve for sigmaemt
        while sum(abs((y1 - y0) ./ y1) >= delta)
            y0 = y1;
            y1(1) = sqrt(fiter1(ng / nrms, BB, y1)); %WATCH for sqrt
            y1(2) = fiter2(ng / nrms, BB, y1);
        end

        Ansx = y1(1);
        Ansy = y1(2);
    end

onesmatrix = ones(size(n .* B));
[sigmaxxemt, sigmaxyemt] = arrayfun(@(nn, BB) solve(nn, BB, 1e-6), onesmatrix .* n,
    onesmatrix .* B);

end
```

```
function Ans = sigmasimple(n, mu, nshift)

if nargin < 3 || isempty(nshift), nshift = 0; end
Ans = abs(n - nshift).*mu
```

Appendix B

Sample RRN code

Here we show a sample of the RRN code that outputs the equivalent resistance for a given carrier density profile and magnetic field in addition to parameters that set the resistance of each four terminal resistor. The essence of this code is to solve a large number of simultaneous equations (Kirchoff's laws, Ohm's law and voltage drops summing to applied voltage) for the RRN. The output is the resistivity of the entire network.

```
function[r_eq] = fourterminal_r_eq(nsd,nmean,H,gg,constant)

%Size of random resistor network
N=40;
M=40;

%Mobility variance and mean - change nonconstant mobility cases.
musd = 0;
mumean = 1;

%Arbitrary V at one edge
Vx=1;

    if (nargin<6)||isempty(gg)||isempty(constant),
        constant=0.35; %called 'c' in PL PRB
        gg=1; %called 'g(phi)' in PL PRB
    end

    rng(0,'twister')
    muValues=musd.*randn(1,N*M) + mumean;

    rng(0,'twister')
    nValues = nsd.*(randn(1,N*M)).^2 + nmean;

    eValues = ones(size(muValues));
```

```
26
27      rhoValues = abs(1./(nValues.*muValues.*eValues));
28
29      t=1;
30      rValues=rhoValues./(pi*t);
31
32      BValues = muValues.*H;
33
34      phi=0.14;
35      g=gg/phi; .
36
37      %a=-g+(pi/4)*B;
38          aValues= -g+(pi/4).*BValues;
39      %b=g+(pi/4)*B;
40          bValues= g+(pi/4).*BValues;
41      %c=0.35-(pi/4)*B;
42          cValues=constant-(pi/4).*BValues;
43      %d=-0.35-(pi/4)*B;
44          dValues=-constant-(pi/4).*BValues;
45
46  %coefficients matrix
47      CoeffsMatrix=zeros(8*N*M,8*N*M);
48
49  %constants matrix
50      ConstantsMatrix=zeros(8*N*M,1);
51      ConstantsMatrix(4*N*M-N+1:4*N*M)=Vx;
52
53  %equations
54
55  %x direction equations
56  %ix equations: i3 of resistor = -i1 of next resistor in each row
57  %There are N*(M-1) ix equations
58
59          m=2*N*M+1; %This is where the i3 list begins i.e. i3(1,1), i2(1,2)
60          for j=1:N
61              for n=(j-1)*(M-1)+1:j*(M-1)
62                      CoeffsMatrix(n,m)=1;
63                      CoeffsMatrix(n,m-2*N*M+1)=1;
64                      m=m+1;
65              end
66              m=m+1;
67          end
68
69
70  %vx equations: v3 of resistor = v1 of next resistor in each row
71  %There are N*(M-1) vx equations
72
73          m=6*N*M+1;
74          for j=1:N
75              for n=1+(j-1)*(M-1)+N*(M-1):j*(M-1)+N*(M-1)
76                      CoeffsMatrix(n,m)=1;
```

```
77                      CoeffsMatrix(n,m-2*N*M+1)=-1;
78                m=m+1;
79              end
80              m=m+1;
81          end
82
83  %y direction equations
84  %iy equations: i4 of resistor=-i2 of next resistor in each column
85  %There are M*(N-1) iy equations
86
87           m=3*N*M+1;
88              for n=2*N*(M-1)+1:2*N*(M-1)+M*(N-1)
89                  CoeffsMatrix(n,m)=1;
90                  CoeffsMatrix(n,m-2*N*M+M)=1;
91                  m=m+1;
92              end
93
94
95  %vy equations: v4 of resistor=v2 of next resistor in each column
96  %There are M*(N-1) vy equations
97
98           m=7*N*M+1;
99              for n=2*N*(M-1)+M*(N-1)+1:2*N*(M-1)+2*M*(N-1)
100                 CoeffsMatrix(n,m)=1;
101                 CoeffsMatrix(n,m-2*N*M+M)=-1;
102                 m=m+1;
103             end
104
105
106
107 %boundary equations
108 %i top equations: i2 of top row = 0
109 %there are M itop equations
110
111         m=N*M+1;
112             for n=(2*N*(M-1)+2*M*(N-1))+1:(2*N*(M-1)+2*M*(N-1)+M)
113                 CoeffsMatrix(n,m)=1;
114                 m=m+1;
115             end
116
117 %i bottom equations: i4 of bottom row = 0
118 %there are M ibottom equations
119
120         m=4*N*M-M+1;
121             for n=2*N*(M-1)+2*M*(N-1)+M+1:4*N*M-2*N
122                 CoeffsMatrix(n,m)=1;
123                 m=m+1;
124             end
125
126 %i boundary equations: i1 of left column = -i3 of right column
127 %there are N-1 iboundary equations
```

```
128
129         m=1;
130         for n=1+4*N*M-2*N:4*N*M-N-1
131             CoeffsMatrix(n,m)=1;
132             CoeffsMatrix(n,m+2*N*M+M-1)=1;
133             m=m+M;
134         end
135
136 %setting a reference V: top left v1 = 0
137
138      CoeffsMatrix(4*N*M-N,4*N*M+1)=1;
139
140 %V row sum equations: (v2-v1)+(v3-v2) across each row = V
141 %there are N Vrow sum equations
142
143         m=4*N*M+1;
144         for n=4*N*M-N+1:4*N*M
145             for j = m:m+M-1
146             CoeffsMatrix(n,j)=-1;
147             CoeffsMatrix(n,j+2*N*M )=1;
148             end
149             m=m+M;
150         end
151
152
153 %KCL equations: i1+i2+i3+i4 at each resistor=0
154 %there are N*M KCL equations
155
156     m=1;
157     for n=4*M*N+1:5*M*N
158         CoeffsMatrix(n,m)=1; %i1
159         CoeffsMatrix(n,m+N*M)=1; %i2
160         CoeffsMatrix(n,m+2*N*M)=1; %i3
161         CoeffsMatrix(n,m+3*N*M)=1; %i4
162         m=m+1;
163     end
164
165 %Resistivity Matrix equations
166 %There are 3*N*M RMatrix equations
167
168             m=1;
169             for n=5*M*N+1:3:8*M*N
170                 CoeffsMatrix(n,m)=rValues(m)*aValues(m); %first i1
171                 CoeffsMatrix(n,m+N*M)=rValues(m)*bValues(m); %first i2
172                 CoeffsMatrix(n,m+2*N*M)=rValues(m)*cValues(m); %first i3
173                 CoeffsMatrix(n,m+3*N*M)=rValues(m)*dValues(m); %first i4
174                 CoeffsMatrix(n,m+4*N*M)=1; %v1
175                 CoeffsMatrix(n,m+5*N*M)=-1; %v2
176
177                 CoeffsMatrix(n+1,m)=rValues(m)*dValues(m); %second i1
178                 CoeffsMatrix(n+1,m+N*M)=rValues(m)*aValues(m); %second i2
```

```
                CoeffsMatrix(n+1,m+2*N*M)=rValues(m)*bValues(m); %second i3
                CoeffsMatrix(n+1,m+3*N*M)=rValues(m)*cValues(m); %second i4
                CoeffsMatrix(n+1,m+5*N*M)=1; %v2
                CoeffsMatrix(n+1,m+6*N*M)=-1; %v3

                CoeffsMatrix(n+2,m)=rValues(m)*cValues(m); %third i1
                CoeffsMatrix(n+2,m+N*M)=rValues(m)*dValues(m); %third i2
                CoeffsMatrix(n+2,m+2*N*M)=rValues(m)*aValues(m); %third i3
                CoeffsMatrix(n+2,m+3*N*M)=rValues(m)*bValues(m); %third i4
                CoeffsMatrix(n+2,m+6*N*M)=1; %v3
                CoeffsMatrix(n+2,m+7*N*M)=-1; %v4

                m=m+1;
            end

%FINAL CALCULATIONS
S=sparse(CoeffsMatrix);

Values=S\ConstantsMatrix;
SumInputI=sum(Values(2*N*M+M:M:3*N*M));
r_eq=Vx/SumInputI;

end
```

Bibliography

[1] Jinglei Ping, Indra Yudhistira, Navneeth Ramakrishnan, Sungjae Cho, Shaffique Adam, and Michael S Fuhrer. Disorder-induced magnetoresistance in a two-dimensional electron system. *Phys. Rev. Lett.*, 113(4):047206, 2014.

[2] Navneeth Ramakrishnan, Mirco Milletari, and Shaffique Adam. Transport and magnetotransport in three-dimensional Weyl semimetals. *Phys. Rev. B*, 92(24):245120, 2015.

[3] Jack Hellerstedt, Mark T Edmonds, Navneeth Ramakrishnan, Chang Liu, Bent Weber, Anton Tadich, Kane M O'Donnell, Shaffique Adam, and Michael S Fuhrer. Electronic properties of high-quality epitaxial topological Dirac semimetal thin films. *Nano Lett.*, 16(5):3210–3214, 2016.

[4] Navneeth Ramakrishnan, Ying Tong Lai, Silvia Lara, and Shaffique Adam. Universality of disorder induced magnetoresistance. *in preparation.*

[5] Peter A Grünberg. Nobel Lecture: From spin waves to giant magnetoresistance and beyond. *Rev. Mod. Phys.*, 80(4):1531, 2008.

[6] DAG Bruggeman. Berechnung verschiedener physikalischer Konstanten von heterogenen Substanzen. I. Dielektrizitätskonstanten und Leitfähigkeiten der Mischkörper aus isotropen Substanzen. *Annalen der physik*, 416(7):636–664, 1935.

[7] Rolf Landauer. Electrical conductivity in inhomogeneous media. In *Electrical transport and optical properties of inhomogeneous media*, volume 40, pages 2–45. AIP Publishing, 1978.

[8] D Stroud and FP Pan. Magnetoresistance and Hall coefficient of inhomogeneous metals. *Phys. Rev. B*, 20(2):455, 1979.

[9] MM Parish and PB Littlewood. Non-saturating magnetoresistance in heavily disordered semiconductors. *Nature*, 426(6963):162–165, 2003.

[10] KSA Novoselov, Andre K Geim, SV Morozov, D Jiang, MI Katsnelson, IV Grigorieva, SV Dubonos, and AA Firsov. Two-dimensional gas of massless Dirac fermions in graphene. *Nature*, 438(7065):197–200, 2005.

[11] Hongbo Gu, Xi Zhang, Huige Wei, Yudong Huang, Suying Wei, and Zhanhu Guo. An overview of the magnetoresistance phenomenon in molecular systems. *Chem. Soc. Rev.*, 42(13):5907–5943, 2013.

[12] W Thomson. On the electro-dynamic qualities of metals: Effects of magnetization on the electric conductivity of Nickel and of Iron. *Proceedings of the Royal Society of London*, 8:546–550, 1856.

[13] T McGuire and RL Potter. Anisotropic magnetoresistance in ferromagnetic 3d alloys. *IEEE Transactions on Magnetics*, 11(4):1018–1038, 1975.

[14] JN Eckstein, I Bozovic, J O'Donnell, M Onellion, and MS Rzchowski. Anisotropic magnetoresistance in tetragonal la1- xcaxmnoδ thin films. *App. Phys. Lett.*, 69(9): 1312–1314, 1996.

[15] Mario Norberto Baibich, Jean Marc Broto, Albert Fert, F Nguyen Van Dau, Frédéric Petroff, P Etienne, G Creuzet, A Friederich, and J Chazelas. Giant magnetoresistance of (001)Fe/(001) Cr magnetic superlattices. *Phys. Rev. Lett.*, 61(21):2472, 1988.

[16] AE Berkowitz, JR Mitchell, MJ Carey, AP Young, Shufeng Zhang, FE Spada, FT Parker, A Hutten, and G Thomas. Giant magnetoresistance in heterogeneous Cu-Co alloys. *Phys. Rev. Lett.*, 68(25):3745, 1992.

[17] HAM van den Berg, Reinder Coehoorn, MAM Gijs, P Grünberg, T Rasing, K Röll, and U Hartmann. *Magnetic multilayers and giant magnetoresistance: fundamentals and industrial applications*, volume 37. Springer Science & Business Media, 2013.

[18] C Gould, C Rüster, T Jungwirth, E Girgis, GM Schott, R Giraud, K Brunner, G Schmidt, and LW Molenkamp. Tunneling anisotropic magnetoresistance: a spin-valve-like tunnel magnetoresistance using a single magnetic layer. *Phys. Rev. Lett.*, 93(11):117203, 2004.

[19] Shinji Yuasa, Taro Nagahama, Akio Fukushima, Yoshishige Suzuki, and Koji Ando. Giant room-temperature magnetoresistance in single-crystal Fe/MgO/Fe magnetic tunnel junctions. *Nat. Mater.*, 3(12):868–871, 2004.

[20] Shinji Yuasa, Akio Fukushima, Taro Nagahama, Koji Ando, and Yoshishige Suzuki. High tunnel magnetoresistance at room temperature in fully epitaxial Fe/MgO/Fe tunnel junctions due to coherent spin-polarized tunneling. *Japanese Journal of Applied Physics*, 43(4B):L588, 2004.

[21] BL Altshuler, D Khmel'Nitzkii, AI Larkin, and PA Lee. Magnetoresistance and Hall effect in a disordered two-dimensional electron gas. *Phys. Rev. B*, 22(11):5142, 1980.

[22] R von Helmolt, J Wecker, B Holzapfel, L Schultz, and K Samwer. Giant negative magnetoresistance in perovskitelike $La_{2/3}Ba_{1/3}MnO_x$ ferromagnetic films. *Phys. Rev. Lett.*, 71(14):2331, 1993.

[23] A Houghton, JR Senna, and SC Ying. Magnetoresistance and hall effect of a disordered interacting two-dimensional electron gas. *Phys. Rev. B*, 25(4):2196, 1982.

[24] Boris L Altshuler, Arkadi G Aronov, and PA Lee. Interaction effects in disordered Fermi systems in two dimensions. *Phys. Rev. Lett.*, 44(19):1288, 1980.

[25] AA Abrikosov. Quantum magnetoresistance. *Phys. Rev. B*, 58(5):2788, 1998.

[26] FV Tikhonenko, AA Kozikov, AK Savchenko, and RV Gorbachev. Transition between electron localization and antilocalization in graphene. *Phys. Rev. Lett.*, 103 (22):226801, 2009.

[27] Mario Novak, Satoshi Sasaki, Kouji Segawa, and Yoichi Ando. Large linear magnetoresistance in the Dirac semimetal TlBiSSe. *Phys. Rev. B*, 91(4):041203, 2015.

[28] *Measuring magnetic fields*. NDT Resource Center. URL https://www.nde-ed.org/educationresources/communitycollege/magparticle/graphics/halleffect.jpg.

[29] *Derek Ho (private communication)*.

[30] David Jeffrey Griffiths and Reed College. *Introduction to electrodynamics*, volume 3. prentice Hall Upper Saddle River, NJ, 1999.

[31] NW Ashcroft and ND Mermin. *Solid State Physics*. Saunders College, Philadelphia, 1976.

[32] S Das Sarma, Shaffique Adam, EH Hwang, and Enrico Rossi. Electronic transport in two-dimensional graphene. *Rev. Mod. Phys.*, 83(2):407, 2011.

[33] AH Castro Neto, F Guinea, Nuno MR Peres, Kostya S Novoselov, and Andre K Geim. The electronic properties of graphene. *Rev. Mod. Phys.*, 81(1):109, 2009.

[34] Andre Konstantin Geim. Graphene: Status and prospects. *Science*, 324(5934):1530–1534, 2009.

[35] IW Frank, David M Tanenbaum, AM Van der Zande, and Paul L McEuen. Mechanical properties of suspended graphene sheets. *Journal of Vacuum Science & Technology B*, 25(6):2558–2561, 2007.

[36] Matthew J Allen, Vincent C Tung, and Richard B Kaner. Honeycomb carbon: a review of graphene. *Chemical Reviews*, 110(1):132–145, 2009.

[37] LA Falkovsky. Optical properties of graphene. In *Journal of Physics: Conference Series*, volume 129, page 012004. IOP Publishing, 2008.

[38] Philip Richard Wallace. The band theory of graphite. *Physical Review*, 71(9):622, 1947.

[39] Jens Martin, N Akerman, G Ulbricht, T Lohmann, JH v Smet, K Von Klitzing, and Amir Yacoby. Observation of electron-hole puddles in graphene using a scanning single-electron transistor. *Nature Physics*, 4(2):144–148, 2008.

[40] Rakesh P Tiwari and D Stroud. Model for the magnetoresistance and hall coefficient of inhomogeneous graphene. *Phys. Rev. B*, 79:165408, Apr 2009. doi: 10.1103/PhysRevB.79.165408. URL http://link.aps.org/doi/10.1103/PhysRevB.79.165408.

[41] Sungjae Cho and Michael S Fuhrer. Charge transport and inhomogeneity near the minimum conductivity point in graphene. *Phys. Rev. B*, 77(8):081402, 2008.

[42] Shaffique Adam, EH Hwang, VM Galitski, and S Das Sarma. A self-consistent theory for graphene transport. *Proceedings of the National Academy of Sciences*, 104(47):18392–18397, 2007.

[43] Sangjun Jeon, Brian B Zhou, Andras Gyenis, Benjamin E Feldman, Itamar Kimchi, Andrew C Potter, Quinn D Gibson, Robert J Cava, Ashvin Vishwanath, and Ali Yazdani. Landau quantization and quasiparticle interference in the three-dimensional Dirac semimetal Cd_3As_2. *Nat. Mater.*, 13(9):851–856, 2014.

[44] X Wan, AM Turner, A Vishwanath, and SY Savrasov. Topological semimetal and Fermi-arc surface states in the electronic structure of pyrochlore iridates. *Phys. Rev. B*, 83(20):205101, 2011.

[45] Z Wang, Y Sun, XQ Chen, C Franchini, G Xu, H Weng, X Dai, and Z Fang. Dirac semimetal and topological phase transitions in A_3Bi (A = Na, K, Rb). *Phys. Rev. B*, 85(19):195320, 2012.

[46] AA Burkov and Leon Balents. Weyl semimetal in a topological insulator multilayer. *Phys. Rev. Lett.*, 107(12):127205, 2011.

[47] Sergey Borisenko, Quinn Gibson, Danil Evtushinsky, Volodymyr Zabolotnyy, Bernd Büchner, and Robert J. Cava. Experimental realization of a three-dimensional Dirac semimetal. *Phys. Rev. Lett.*, 113:027603, Jul 2014.

[48] M Ali, Q Gibson, S Jeon, B Zhou, A Yazdani, and R Cava. The crystal and electronic structures of Cd_3As_2, the three-dimensional electronic analogue of graphene. *Inorg. Chem.*, 53(8):4062–4067, 2014.

[49] T Liang, Q Gibson, M Ali, M Liu, R Cava, and N Ong. Ultrahigh mobility and giant magnetoresistance in the Dirac semimetal Cd_3As_2. *Nat. Mater.*, 2014.

[50] Su-Yang Xu, Ilya Belopolski, Nasser Alidoust, Madhab Neupane, Guang Bian, Chenglong Zhang, Raman Sankar, Guoqing Chang, Zhujun Yuan, Chi-Cheng Lee, et al. Discovery of a Weyl Fermion semimetal and topological Fermi arcs. *Science*, 349 (6248):613–617, 2015.

[51] Suyang Xu, Y Xia, LA Wray, S Jia, F Meier, JH Dil, J Osterwalder, B Slomski, A Bansil, H Lin, R Cava, and M. Z. Hasan. Topological phase transition and texture inversion in a tunable topological insulator. *Science*, 332(6029):560–564, 2011.

[52] B Singh, A Sharma, H Lin, MZ Hasan, R Prasad, and A Bansil. Topological electronic structure and Weyl semimetal in the $TlBiSe_2$ class of semiconductors. *Phys. Rev. B*, 86(11):115208, 2012.

[53] Q Gibson, L Schoop, L Muechler, L Xie, M Hirschberger, N Ong, R Car, and RJ Cava. Three-dimensional Dirac semimetals: Design principles and predictions of new materials. *Phys. Rev. B*, 91(20):205128, 2015.

[54] Y Ominato and M Koshino. Quantum transport in a three-dimensional Weyl electron system. *Phys. Rev. B*, 89(5):054202, 2014.

[55] Björn Sbierski, Gregor Pohl, Emil J Bergholtz, and Piet W Brouwer. Quantum transport of disordered Weyl semimetals at the nodal point. *Phys. Rev. Lett.*, 113: 026602, Jul 2014.

[56] Rex Lundgren, Pontus Laurell, and Gregory A Fiete. Thermoelectric properties of Weyl and Dirac semimetals. *Phys. Rev. B*, 90(16):165115, 2014.

[57] S Das Sarma, EH Hwang, and Hongki Min. Carrier screening, transport, and relaxation in three-dimensional Dirac semimetals. *Phys. Rev. B*, 91(3):035201, 2015.

[58] AA Burkov. Chiral anomaly and diffusive magnetotransport in Weyl metals. *Phys. Rev. Lett.*, 113(24):247203, 2014.

[59] RR Biswas and Shinsei Ryu. Diffusive transport in Weyl semimetals. *Phys. Rev. B*, 89:014205, Jan 2014.

[60] William Witczak-Krempa, Michael Knap, and Dmitry Abanin. Interacting Weyl Semimetals: Characterization via the topological Hamiltonian and its breakdown. *Phys. Rev. Lett.*, 113:136402, Sep 2014.

[61] Brian Skinner. Coulomb disorder in three-dimensional Dirac systems. *Phys. Rev. B*, 90(6):060202, 2014.

[62] L Min and SC Zhang. Dielectric function, Friedel oscillation and plasmons in Weyl semimetals. *Int. J. Mod. Phys. B*, 27(25), 2013.

[63] *Michael Fuhrer (private communication).*

[64] Shaffique Adam and S Das Sarma. Boltzmann transport and residual conductivity in bilayer graphene. *Phys. Rev. B*, 77(11):115436, 2008.

[65] AA Burkov, MD Hook, and Leon Balents. Topological nodal semimetals. *Phys. Rev. B*, 84(23):235126, 2011.

[66] John M Ziman. *Models of disorder: The theoretical physics of homogeneously disordered systems*. CUP Archive, 1979.

[67] Q Li, EH Hwang, and E Rossi. Effect of charged impurity correlations on transport in monolayer and bilayer graphene. *Solid State Commun.*, 152(15):1390–1399, 2012.

[68] Jingshi Hu, Meera M Parish, and TF Rosenbaum. Nonsaturating magnetoresistance of inhomogeneous conductors: Comparison of experiment and simulation. *Phys. Rev. B*, 75(21):214203, 2007.

[69] Takahiro Morimoto and Akira Furusaki. Weyl and Dirac semimetals with Z_2 topological charge. *Phys. Rev. B*, 89(23):235127, 2014.